University of Groningen

Master Research Project Physics

Probing Annihilation Topologies in $B^+ \to J/\psi\pi^+$ and $B^+ \to J/\psi K^+$

Author:
Huy Banh *(S4228561)*

First Supervisor:
Dr. K. De Bruyn
Second Supervisor:
Prof. dr. R. Fleischer

June 17, 2026

Abstract

Precision studies of the B-meson system provide sensitive tests of the Standard Model. In particular, a precise determination of the B_d^0–$\bar{B}_d^0$ mixing phase ϕ_d requires reliable control of subleading decay topologies, since their effects could otherwise be mistaken for new-physics effects. In this thesis, we extend an established global-fit strategy, implemented within `GammaCombo`, by including annihilation topologies in the charged control modes $B^+ \to J/\psi\pi^+$ and $B^+ \to J/\psi K^+$ and investigate their impact on ϕ_d.

Using only measurements of CP asymmetries, the resulting fit becomes underconstrained once annihilation contributions are included, so the associated hadronic parameters cannot be determined uniquely. Including the ratio of CP-averaged branching fractions significantly improves the constraints when the relevant hadronic amplitude ratio is imposed as a Gaussian constraint, making it possible to determine the hadronic parameters uniquely. To quantify the impact on ϕ_d, we compare the fitted value of ϕ_d with and without annihilation topologies and find that the central value is shifted by only $\delta\phi_d = 0.03°$. As a cross-check, we also develop a fixed-point strategy, in which the annihilation parameters are fixed point-by-point across the parameter space. This strategy can be applied more generally in cases where a direct determination of the hadronic parameters is not feasible. In this approach, the systematic uncertainty on ϕ_d associated with annihilation topologies corresponds to about 10% of the 68% experimental interval width. We therefore conclude that annihilation contributions are negligible given the current experimental precision on ϕ_d, even with projected end-of-HL-LHC and Belle II precision.

Contents

1 Introduction **4**

2 Overview of Decay Topologies **7**

3 Global Fit **9**
3.1 Fit Strategy . . . 9
3.2 CP-Violating Observables . . . 10
3.3 General Amplitude Parametrization . . . 11
3.4 Parametrization of the B^+ Modes . . . 12
3.4.1 $B^+ \to J/\psi\pi^+$ . . . 12
3.4.2 $B^+ \to J/\psi K^+$ . . . 13
3.4.3 U-spin Relation . . . 13

4 Effective Weak Hamiltonian **14**
4.1 Operator Product Expansion . . . 14
4.2 Factorization . . . 17
4.2.1 Color-Allowed Tree Topology . . . 17
4.2.2 Color-Suppressed Tree Topology . . . 20
4.3 Full Effective Hamiltonian for $|\Delta B|= 1$, $\Delta C = 0$ Decays . . . 21

5 Branching Fraction Ratios **23**
5.1 General Relations for Two-Body Decays . . . 23
5.2 Application to $B^+ \to J/\psi\pi^+$ and $B^+ \to J/\psi K^+$ . . . 24
5.2.1 U-spin Breaking in ξ . . . 24
5.2.2 Benchmark Scenarios for ξ . . . 25
5.2.3 Ratio of Direct CP Asymmetries . . . 27

6 Methodology **29**
6.1 E+A Fit . . . 30
6.2 E+A+R Fit . . . 32
6.3 Future Projections . . . 32
6.4 Experimental Inputs . . . 33

7 Fit Results **34**
7.1 Nominal and Extended Fits . . . 34
7.2 E+A Fit . . . 36
7.2.1 Floating-fit Results . . . 36
7.2.2 Fixed-point Results . . . 39
7.3 E+A+R Fit . . . 41
7.3.1 $\xi^{\mathcal{R}}$ as a Free Parameter . . . 41
7.3.2 $\xi^{\mathcal{R}}$ as a Gaussian Constraint . . . 43
7.4 Future Projections . . . 46
7.4.1 Extended Fit . . . 46
7.4.2 E+A Fit . . . 48
7.4.3 E+A+R Fit . . . 52

8 Conclusion **57**

Acknowledgements **58**

References **59**

A Decay Rate Derivation **63**

B Derivation Kinematic Factor **65**

C Determination $f_{B\to\pi}^{+}(m_{J/\psi}^{2})$ **67**

D GammaCombo Combiner Module **68**

E Future Projections **69**
E.1 Extended and E+A Fit 69
E.2 E+A+R Fit 70

1 Introduction

The Standard Model (SM) provides a highly successful description of elementary particles and their interactions. Despite this success, it is widely understood to be incomplete. For example, it does not account for dark matter, does not include gravity, and does not fully explain the observed dominance of matter over antimatter in the universe [1], [2]. These limitations motivate the broader search for physics beyond the SM. One way to look for possible signs of such physics is through precision measurements, where experimentally determined observables are compared with their SM predictions. Deviations between the two may indicate additional contributions from new physics [3].

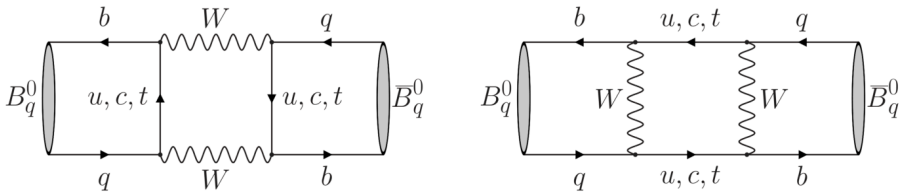

Figure 1: Standard Model box diagrams for the B_q^0–$\bar{B}_q^0$ process. Figure taken from Ref. [4].

An important observable in this context is the phase ϕ_d, which governs B_d^0–$\bar{B}_d^0$ mixing in the neutral B_d^0-meson system. In the SM, this mixing is mediated by loop-level box diagrams, as shown in Fig. 1. The SM prediction for this phase is related to the unitarity triangle through [5]

$$\phi_d^{\mathrm{SM}} = 2\beta, \tag{1}$$

where β is one of the angles of the unitarity triangle shown in Fig. 2. Assuming CKM unitarity, β can in turn be determined from R_b and γ [6].

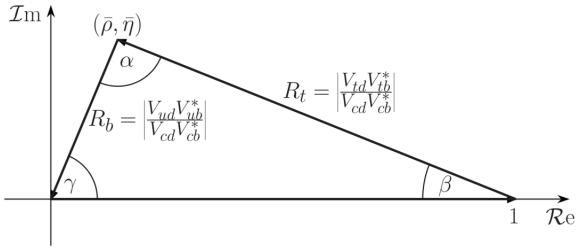

Figure 2: The unitarity triangle, which follows from the unitarity of the CKM matrix. Figure taken from Ref. [4].

The phase ϕ_d is of particular interest, since the loop-induced nature of B_d^0–$\bar{B}_d^0$ mixing makes this process sensitive to possible contributions from physics beyond the SM [6], for instance from additional heavy particles that may enter the mixing amplitude. A well-known example of such a hypothetical particle is a heavy neutral gauge boson Z' [7]. In general, one may therefore write [5]

$$\phi_d = \phi_d^{\mathrm{SM}} + \phi_d^{\mathrm{NP}}, \tag{2}$$

where ϕ_d^{NP} parametrizes possible contributions from physics beyond the SM.

Experimentally, the decay $B_d^0 \to J/\psi K^0$ plays an important role in probing the mixing phase ϕ_d through its CP asymmetries. Throughout this thesis, the symbol K^0 is used as a shorthand for either K_S^0 or K_L^0. Due to the experimentally clean signature and relatively large branching fraction of this decay mode, it provides the most precise measurements for the determination of ϕ_d and is therefore commonly referred to as the *golden mode* [5]. However, with the current level of experimental precision, the determination of ϕ_d from CP asymmetries requires taking into account not only the dominant tree-level contributions to the decay amplitudes, but also subleading SM contributions [5]. These subleading decay topologies modify the CP asymmetries and thereby shift the phase determined from data [5]. As a result, the experimentally measured quantity is in general an effective phase [5],

$$\phi_{d,f}^{\text{eff}} = \phi_d + \Delta\phi_d^f, \tag{3}$$

where $\Delta\phi_d^f$ denotes the shift induced by subleading SM effects for a given final state f. If such effects are not taken into account properly, they may be mistaken for new-physics contributions [5]. This illustrates the importance of controlling these subleading SM effects in the precision determination of ϕ_d.

In the decay channels considered in this thesis, an important class of subleading effects arises from penguin topologies. To account for these contributions, the decay amplitudes are parametrized in terms of hadronic parameters associated with the subleading decay topologies [5]. This introduces additional degrees of freedom into the analysis: besides the mixing phase ϕ_d, one must also constrain the hadronic parameters describing the penguin contributions.

For this reason, additional information from control modes is needed in order to obtain a sufficiently constrained system. Through $\text{SU}(3)_\text{F}$ flavor symmetry, i.e. the approximate symmetry among the light quarks u, d, and s [8], the hadronic parameters of channels with similar hadronic dynamics can be related to one another, such that observables from control modes provide complementary constraints on the same underlying hadronic quantities [5]. By combining the observables of different modes in a global fit, one can constrain the subleading hadronic contributions simultaneously with the phase ϕ_d.

In principle, the most suitable control mode is $B_s^0 \to J/\psi K^0$ [5], which is related to the golden mode through U-spin, the SU(2) subgroup of $\text{SU}(3)_\text{F}$ corresponding to the interchange $d \leftrightarrow s$ [8]. Due to the one-to-one correspondence between the contributing decay topologies in these two channels, this mode is theoretically the cleanest partner of $B_d^0 \to J/\psi K^0$ [5]. However, given the current limited experimental precision of the CP-asymmetry measurements in $B_s^0 \to J/\psi K_S^0$, it is important to consider additional control modes as well [5].

Another natural candidate is $B_d^0 \to J/\psi \pi^0$ [5]. Similar to $B_d^0 \to J/\psi K^0$ and $B_s^0 \to J/\psi K^0$, this decay belongs to the class of $B \to J/\psi P$ modes, where P denotes a light pseudoscalar meson. It can therefore provide complementary information on the hadronic parameters associated with penguin topologies. However, compared to $B_s^0 \to J/\psi K^0$, this mode introduces additional theoretical complexity. In particular, the correspondence with the golden mode is no longer one-to-one, since $B_d^0 \to J/\psi \pi^0$ receives additional contributions from penguin-annihilation and exchange topologies that are absent in $B_d^0 \to J/\psi K^0$ [5].

Other interesting candidates are the charged decays $B^+ \to J/\psi\pi^+$ and $B^+ \to J/\psi K^+$. These modes are also governed by similar hadronic dynamics and can provide additional constraints. However, since charged B mesons do not undergo mixing, these modes contribute only through direct CP asymmetries and therefore have to be used in addition to other control modes [5]. Moreover, the correspondence with the golden mode is also not one-to-one, since annihilation topologies enter the charged modes in addition to the tree and penguin topologies, but are absent in $B_d^0 \to J/\psi K^0$ [5].

The exchange, penguin-annihilation, and annihilation topologies are generally expected to be suppressed relative to the penguin contributions, following the usual hierarchy of decay topologies, and are therefore often neglected [9]. However, the steadily increasing experimental precision raises the question of whether these additional subleading effects can still be neglected reliably.

Since annihilation topologies are the only additional topologies beyond the penguin topologies in the B^+ modes and admit a straightforward parametrization, this thesis uses the B^+ modes as a case study for studying the potential impact of decay topologies beyond the penguin contributions on the determination of ϕ_d. To probe the sensitivity to annihilation contributions in a controlled way, we focus on annihilation topologies in isolation and therefore neglect exchange and penguin-annihilation topologies.

This leads to the following central questions addressed in this thesis:

1. What do we know about contributions from annihilation topologies in the modes $B^+ \to J/\psi\pi^+$ and $B^+ \to J/\psi K^+$?

2. What is the resulting impact of these annihilation topologies on the mixing phase ϕ_d?

This thesis is structured as follows. Section 2 provides an overview of decay topologies. Section 3 introduces the starting point of the fitting strategy by discussing the decay modes included in the global fit and the parametrization of the corresponding observables, in particular the CP asymmetries. Section 4 presents the effective weak Hamiltonian and the field-theoretic framework used to describe the hadronic amplitudes and their relations. Section 5 then discusses branching fractions as an additional class of observables that can be incorporated into the global fit. Section 6 introduces the methodology developed in this thesis, including the fit strategies used to account for annihilation topologies. The fit results are presented and discussed in Section 7. Finally, Section 8 summarizes the main conclusions of the thesis.

2 Overview of Decay Topologies

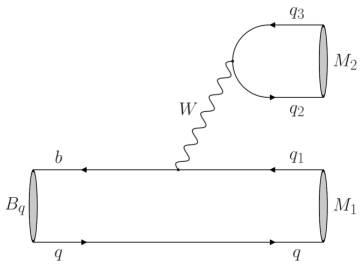

(a) Color-allowed tree topology.

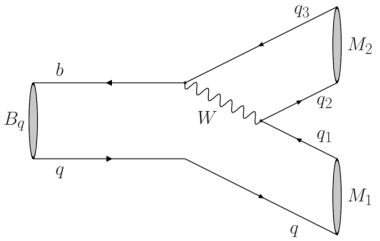

(b) Color-suppressed tree topology.

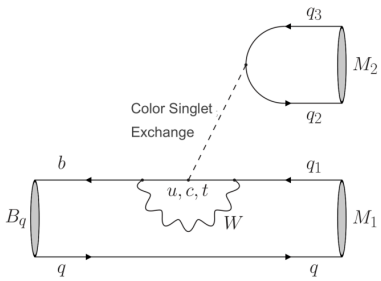

(c) Color-allowed penguin topology.

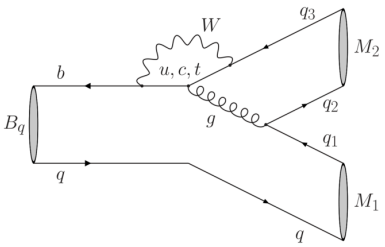

(d) Color-suppressed penguin topology.

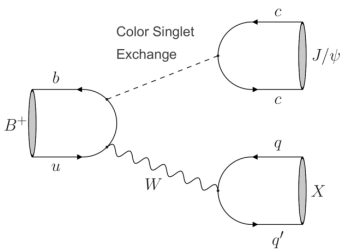

(e) Annihilation topology.

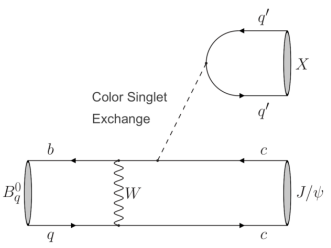

(f) Exchange topology.

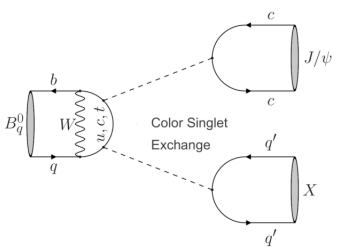

(g) Penguin-annihilation topology.

Figure 3: Overview of decay topologies. Panels (a) and (b) show the leading-order tree topologies contributing to $B_q \to M_1 M_2$ decays mediated by the exchange of a virtual W boson. Panels (c) and (d) show penguin topologies, while panels (e)–(g) show the annihilation, exchange, and penguin-annihilation topologies. Figure adapted from Ref. [4].

Figure 3 provides an overview of the decay topologies for the considered processes, $B_q^0 \to M_1 M_2$ and $B^+ \to J/\psi X^+$.

The leading-order contributions are given by the tree topologies shown in Figs. 3a and 3b. These arise from the exchange of a virtual W boson. Subleading contributions are provided by the penguin topologies shown in Figs. 3c and 3d, which proceed through loop

diagrams. The B^+ modes receive contributions from the annihilation topology shown in Fig. 3e. This topology, as well as the exchange and penguin-annihilation topologies, requires the participation of the spectator quark and is therefore generally expected to be suppressed relative to the penguin topologies [9].

The tree and penguin topologies can be divided further into color-allowed and color-suppressed contributions. This distinction is related to the color structure of the corresponding amplitudes. In the color-allowed case, the $\bar{b} \to \bar{q}_1$ transition proceeds through the emission of a virtual W boson, which produces a $\bar{q}_3 q_2$ pair. Since the W boson is a color singlet, this quark pair is produced in a color-singlet configuration. The quarks $\bar{q}_3$ and q_2 can therefore form one of the final-state mesons, while $\bar{q}_1$ combines with the spectator quark q to form the other meson. In this way, the color flow associated with the two mesons is uncorrelated, allowing the color indices to be summed independently. In the color-suppressed case, however, the color configuration of the quarks produced by the W boson is correlated with that of the $\bar{q}_1$ and spectator quark, since both final-state mesons must be color singlets simultaneously. As a consequence, there is no independent color sum, and the corresponding amplitude is suppressed by a factor of $1/N_c$ with respect to the color-allowed topology, with $N_c = 3$ [4], [10]. This classification is illustrated in Fig. 3 for both the tree and penguin contributions.

3 Global Fit

3.1 Fit Strategy

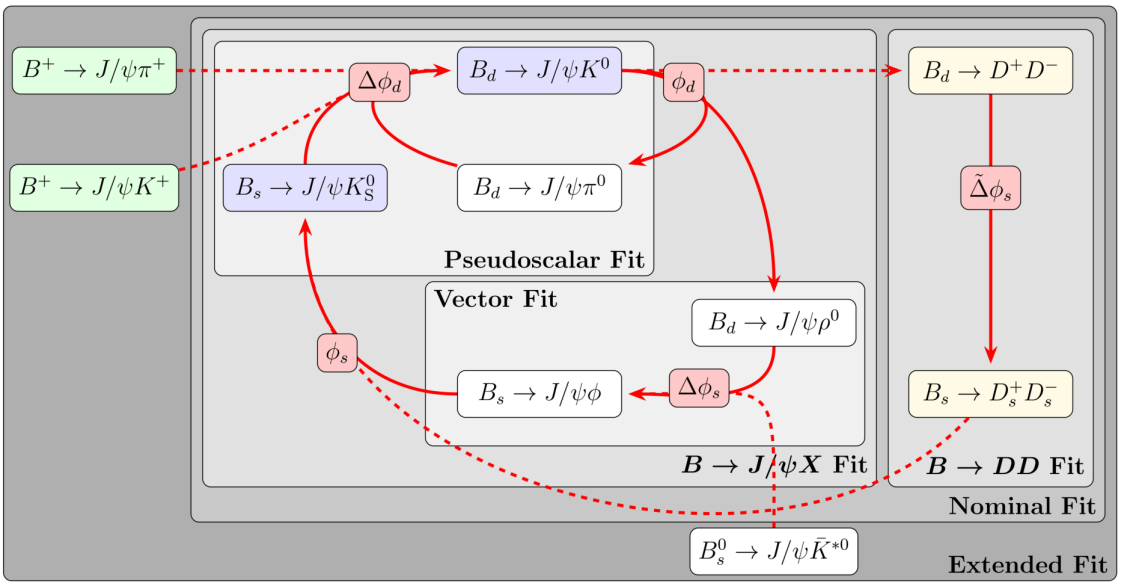

Figure 4: Schematic overview of the fitting strategy of Ref. [5]. Figure taken from Ref. [5].

As a starting point, this work adopts the global-fit methodology of Ref. [5], in which only the leading tree and penguin topologies are taken into account, while other subleading contributions are considered to be negligible, i.e. exchange, penguin-annihilation and annihilation topologies. The experimental input is provided by the CP asymmetries of the decay modes shown in Fig. 4.

The decay modes are grouped into three separate sectors: the Pseudoscalar Fit, the Vector Fit, and the $B \to D\bar{D}$ Fit. These correspond to final states of the type vector+pseudoscalar, vector+vector, and pseudoscalar+pseudoscalar, respectively. This classification reflects the different hadronic dynamics of the corresponding decay classes.

Figure 4 illustrates the structure of the different fit strategies. The Nominal Fit combines the Pseudoscalar Fit, the Vector Fit, and the $B \to D\bar{D}$ Fit. The Extended Fit extends this framework by including additional control modes, namely the charged decays $B^+ \to J/\psi\pi^+$ and $B^+ \to J/\psi K^+$, as well as the $B_s^0 \to J/\psi\bar{K}^{*0}$ mode. Since these final states are not CP eigenstates, they do not give rise to mixing-induced CP asymmetries and are therefore only included in the Extended Fit [5].

Within each sector, $\mathrm{SU(3)_F}$ flavor symmetry is used to relate the hadronic parameters associated with the corresponding subleading decay topologies across the different decay modes. These relations are thus imposed only between modes belonging to the same class of hadronic dynamics.

In each fit strategy, the available experimental inputs are combined in a global fit by constructing a single likelihood function $\mathcal{L}$ as the product of the individual likelihoods $\mathcal{L}_i$ [11]:

$$\mathcal{L}(\vec{\alpha}) = \prod_i \mathcal{L}_i(\vec{\beta}_i), \tag{4}$$

where the product runs over all input measurements. The vectors $\vec{\beta}_i$ contain the parameters relevant for the individual observables, while $\vec{\alpha}$ denotes the full set of fit parameters appearing in the different $\vec{\beta}_i$ [11]. In this work, the minimization of the global likelihood is performed using `GammaCombo`.

The corresponding χ^2 function is defined as [11]

$$\chi^2(\vec{\alpha}) \equiv -2 \ln \mathcal{L}(\vec{\alpha}). \tag{5}$$

Minimization of this χ^2 function yields the best-fit values of the fit parameters. Confidence-level (CL) regions are then constructed from the difference $\Delta\chi^2$ with respect to the minimum. In two-dimensional parameter planes, the 39% and 87% CL contours correspond to the usual 68% and 95% intervals in one-dimensional scans, respectively [11]. Further details of the statistical implementation in `GammaCombo` can be found in Ref. [11].

3.2 CP-Violating Observables

As discussed in the previous subsection, the experimental input to the global fit is provided by CP asymmetries. We therefore begin by introducing the CP-violating observables that enter the fit.

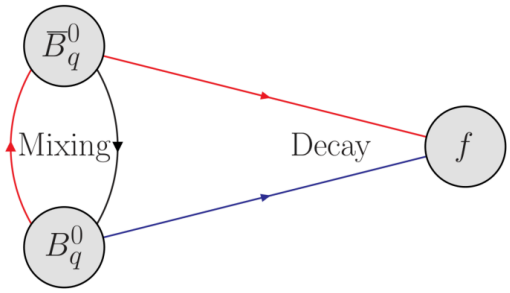

Figure 5: Interference between mixing and decay. Figure taken from Ref. [4].

For all decay modes considered in this work, the direct CP asymmetry is used as an observable. It is defined as [4]

$$\mathcal{A}_{\mathrm{CP}}^{\mathrm{dir}} = \frac{\left|A(B \to f)\right|^2 - \left|A(\bar{B} \to \bar{f})\right|^2}{\left|A(B \to f)\right|^2 + \left|A(\bar{B} \to \bar{f})\right|^2}. \tag{6}$$

For neutral decays of the type $B_q^0 \to f$, where f is a CP eigenstate, an additional observable arises from the interference between mixing and decay [4]. A neutral B_q^0 meson can either decay directly into the final state f or first oscillate into its antiparticle $\bar{B}_q^0$ and subsequently decay into the same final state [12]. The interference between these two decay paths,

illustrated schematically in Fig. 5, gives rise to a time-dependent CP asymmetry [4]. This asymmetry can be written as [5]

$$\begin{aligned} a_{\rm CP}(t) &= \frac{\left|A(B_q^0(t)\to f)\right|^2 - \left|A(\bar{B}_q^0(t)\to f)\right|^2}{\left|A(B_q^0(t)\to f)\right|^2 + \left|A(\bar{B}_q^0(t)\to f)\right|^2} \\ &= \frac{\mathcal{A}_{\rm CP}^{\rm dir}\cos(\Delta m_q t) + \mathcal{A}_{\rm CP}^{\rm mix}\sin(\Delta m_q t)}{\cosh(\Delta\Gamma_q t/2) + \mathcal{A}_{\Delta\Gamma}\sinh(\Delta\Gamma_q t/2)}. \end{aligned} \tag{7}$$

The quantities $\mathcal{A}_{\rm CP}^{\rm dir}$, $\mathcal{A}_{\rm CP}^{\rm mix}$, and $\mathcal{A}_{\Delta\Gamma}$ describe direct CP violation, mixing-induced CP violation, and the contribution associated with the decay-width difference between the heavy and light neutral-B_q mass eigenstates, respectively.

3.3 General Amplitude Parametrization

We now introduce a general parametrization of the decay amplitudes in terms of hadronic parameters that encode the effects of subleading decay topologies. These parameters enter the expressions for the CP-violating observables and are constrained by experimental data through the global-fit framework described in Section 3.1.

For a decay of the type $B_q \to f$, the amplitudes can be written as [5]

$$A(B_q \to f) \equiv \mathcal{N}_f \left[1 - b_f e^{i\rho_f} e^{i\gamma}\right], \tag{8}$$

$$A(\bar{B}_q \to \bar{f}) \equiv \mathcal{N}_{\bar{f}} \left[1 - b_f e^{i\rho_f} e^{-i\gamma}\right], \tag{9}$$

where $\mathcal{N}_f$ is a normalization factor, b_f parametrizes the size of subleading contributions relative to the leading-order tree contribution, ρ_f is the associated strong phase, and γ is the weak-phase difference and unitarity-triangle angle shown in Fig. 2.

Substituting Eq. (8) into Eq. (6) yields [5]

$$\mathcal{A}_{\rm CP}^{\rm dir}(B_q \to f) = \frac{2 b_f \sin\rho_f \sin\gamma}{1 - 2 b_f \cos\rho_f \cos\gamma + b_f^2}. \tag{10}$$

This expression shows that contributions from subleading decay topologies can generate a nonzero direct CP asymmetry. However, for $B \to J/\psi X$ modes, the hierarchy between the leading tree contribution and the subleading penguin amplitudes implies that the resulting value of $\mathcal{A}_{\rm CP}^{\rm dir}$ is expected to be small.

For the mixing-induced CP asymmetry, one finds [5]

$$\eta_f \mathcal{A}_{\rm CP}^{\rm mix}(B_q \to f) = \frac{\sin\phi_q - 2 b_f \cos\rho_f \sin(\phi_q + \gamma) + b_f^2 \sin(\phi_q + 2\gamma)}{1 - 2 b_f \cos\rho_f \cos\gamma + b_f^2}. \tag{11}$$

Equation (11) shows how subleading hadronic contributions, parametrized by b_f and ρ_f, enter the mixing-induced CP asymmetry and affect the determination of the mixing phase ϕ_q. Their effect can be described as a shift in the phase determined from $\mathcal{A}_{\rm CP}^{\rm mix}$. This is captured by the effective phase description in Eq. (3), where the measured phase differs from the underlying mixing phase by the correction $\Delta\phi_q^f$. A precise control of these effects is therefore essential in the global fit.

3.4 Parametrization of the B^+ Modes

We now extend the analysis presented in Section 3.1 by introducing a parametrization of the charged modes $B^+ \to J/\psi\pi^+$ and $B^+ \to J/\psi K^+$ that includes the effects of annihilation topologies.

3.4.1 $B^+ \to J/\psi\pi^+$

For the decay $B^+ \to J/\psi\pi^+$, the amplitude can be written as

$$A = V_{cb}^* V_{cd} T + V_{ub}^* V_{ud} P^{(u)} + V_{cb}^* V_{cd} P^{(c)} + V_{tb}^* V_{td} P^{(t)} + V_{ub}^* V_{ud} A_{\text{ann}}, \tag{12}$$

where T denotes the tree amplitude, $P^{(q)}$ the penguin amplitudes with internal quark q, and A_{ann} the annihilation amplitude.

Using CKM unitarity, this amplitude can be cast into the form of Eq. (8), with [4]

$$\mathcal{N}_{J/\psi\pi^+} = V_{cb}^* V_{cd} \left(T + P^{(c)} - P^{(t)} \right), \tag{13}$$

and

$$b_{J/\psi\pi^+} e^{i\rho_{J/\psi\pi^+}} = a_{\text{sca}} e^{i\theta_{\text{sca}}} + x e^{i\sigma}, \tag{14}$$

where

$$a_{\text{sca}} e^{i\theta_{\text{sca}}} = R_b \frac{P^{(u)} - P^{(t)}}{T + P^{(c)} - P^{(t)}}, \tag{15}$$

$$x e^{i\sigma} = R_b \frac{A_{\text{ann}}}{T + P^{(c)} - P^{(t)}}. \tag{16}$$

Here, $a_{\text{sca}} e^{i\theta_{\text{sca}}}$ and $x e^{i\sigma}$ parametrize the penguin and annihilation contributions, respectively, within the pseudoscalar sector of the global fit. The side R_b of the unitarity triangle (see Fig. 2) is given by

$$R_b \equiv \left| \frac{V_{ud} V_{ub}^*}{V_{cd} V_{cb}^*} \right| = \left(1 - \frac{1}{2}\lambda^2 \right) |\rho + i\eta| + \mathcal{O}(\lambda^4). \tag{17}$$

Substituting Eq. (14) into Eq. (10) yields [4]

$$\mathcal{A}_{\text{CP}}^{\text{dir}} = \frac{2 \left(a_{\text{sca}} \sin\theta_{\text{sca}} + x \sin\sigma \right) \sin\gamma}{1 - 2 \left(a_{\text{sca}} \cos\theta_{\text{sca}} + x \cos\sigma \right) \cos\gamma + 2 a_{\text{sca}} x \cos(\theta_{\text{sca}} - \sigma) + a_{\text{sca}}^2 + x^2}. \tag{18}$$

3.4.2 $B^+ \to J/\psi K^+$

An analogous parametrization can be introduced for the decay $B^+ \to J/\psi K^+$. Its amplitude is given by

$$A = V_{cb}^* V_{cs} T' + V_{ub}^* V_{us} P'^{(u)} + V_{cb}^* V_{cs} P'^{(c)} + V_{tb}^* V_{ts} P'^{(t)} + V_{ub}^* V_{us} A'_{\text{ann}}, \tag{19}$$

with normalization factor

$$\mathcal{N}_{J/\psi K^+} = V_{cb}^* V_{cs} \left(T' + P'^{(c)} - P'^{(t)} \right). \tag{20}$$

The corresponding hadronic parameters are defined as

$$b_{J/\psi K^+} e^{i\rho_{J/\psi K^+}} = -\epsilon \left(a'_{\text{sca}} e^{i\theta'_{\text{sca}}} + x' e^{i\sigma'} \right), \tag{21}$$

where the parameter ϵ is given by

$$\epsilon \equiv \frac{\lambda^2}{1-\lambda^2}, \tag{22}$$

with λ denoting one of the Wolfenstein parameters of the CKM matrix.

The quantities $a'_{\text{sca}} e^{i\theta'_{\text{sca}}}$ and $x' e^{i\sigma'}$ are defined as

$$a'_{\text{sca}} e^{i\theta'_{\text{sca}}} \equiv R_b \frac{P'^{(u)} - P'^{(t)}}{T' + P'^{(c)} - P'^{(t)}}, \tag{23}$$

$$x' e^{i\sigma'} \equiv R_b \frac{A'_{\text{ann}}}{T' + P'^{(c)} - P'^{(t)}}. \tag{24}$$

The corresponding expression for the direct CP asymmetry is obtained from Eq. (18) by applying the substitutions [4]

$$a_{\text{sca}} \to \epsilon a'_{\text{sca}}, \quad \theta_{\text{sca}} \to \theta'_{\text{sca}} + \pi, \quad x \to \epsilon x', \quad \sigma \to \sigma' + \pi. \tag{25}$$

3.4.3 U-spin Relation

The decays $B^+ \to J/\psi \pi^+$ and $B^+ \to J/\psi K^+$ are related by the U-spin transformation $d \leftrightarrow s$. In the limit of exact U-spin symmetry, the corresponding tree, penguin, and annihilation amplitudes are identical, implying [4], [5]

$$a_{\text{sca}} e^{i\theta_{\text{sca}}} = a'_{\text{sca}} e^{i\theta'_{\text{sca}}}, \quad x e^{i\sigma} = x' e^{i\sigma'}. \tag{26}$$

These relations allow the charged control modes to constrain the hadronic parameters entering the global fit.

4 Effective Weak Hamiltonian

In the previous section, we employed a phenomenological parametrization of the decay amplitudes, in which contributions from different decay topologies are encoded in hadronic parameters that are constrained using experimental data. To complement this approach, it is useful to examine how hadronic amplitudes are described from a theoretical point of view. This will be useful for the discussion in Section 5, where branching fraction ratios are introduced as additional observables.

Following the discussion in Ref. [4], we note that weak B-meson decays involve widely separated energy scales. The typical scale of the decay is set by the b-quark mass, $E \sim m_b = 4.183 \pm 0.004$ GeV [13], whereas the weak interaction is mediated by the much heavier W boson, with $m_W = 80.3692 \pm 0.0133$ GeV [13]. Since the relevant decay scale is far below m_W, the exchange of the W boson can be described by a local interaction rather than by resolving the W boson as a propagating particle [4]. This motivates the use of a low-energy effective field theory, in which the W boson and other heavy degrees of freedom are integrated out [14]. The resulting effective weak Hamiltonian provides the framework for describing non-leptonic B-meson decays.

4.1 Operator Product Expansion

The decay amplitude for a transition from an initial state $|i\rangle$ to a final state $|f\rangle$ is obtained from the matrix element of the effective Hamiltonian,

$$A = \langle f|\mathcal{H}_{\text{eff}}|i\rangle. \tag{27}$$

To describe this amplitude, we first derive the low-energy effective Hamiltonian $\mathcal{H}_{\text{eff}}$ for the weak transition $pq \to p'q'$, following the general reasoning in Ref. [4]. This transition is visualized in Fig. 6.

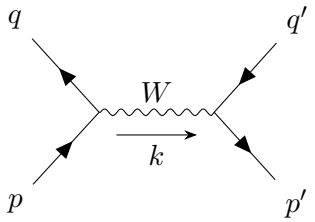

Figure 6: Leading-order Feynman diagram for the weak transition $pq \to p'q'$ in the full Standard Model, mediated by a virtual W boson with momentum k.

In the Operator Product Expansion (OPE) framework, the effective Hamiltonian is expanded in a basis of local operators $\mathcal{O}_j$ with Wilson coefficients C_j [15]:

$$\mathcal{H}_{\text{eff}} = \frac{G_F}{\sqrt{2}} V_{pq}^* V_{p'q'} \sum_j C_j(\mu)\mathcal{O}_j(\mu), \tag{28}$$

where both C_j and $\mathcal{O}_j$ depend on the renormalization scale μ, and G_F is the Fermi constant [15].

The scale μ separates the high-energy (short-distance) contributions, captured by the Wilson coefficients C_j, from the low-energy (long-distance) dynamics contained in the hadronic matrix elements $\langle f|\mathcal{O}_j|i\rangle$ [16]. Importantly, the physical amplitude should be independent of the renormalization scale [16].

To determine the corresponding Wilson coefficients, we start from the Standard Model Hamiltonian at the matching scale $\mu = m_W$. Due to the asymptotic freedom of QCD, the $\mathrm{SU(3)_C}$ gauge coupling $\alpha_s(\mu)$ is small at this scale. Hence, the coefficients can be calculated using perturbation theory at this scale by matching the full Standard Model theory with the effective Hamiltonian [15]:

$$\langle f|\mathcal{H}_{\mathrm{SM}}(m_W)|i\rangle = \langle f|\mathcal{H}_{\mathrm{eff}}(m_W)|i\rangle. \tag{29}$$

To illustrate this, we first perform tree-level matching where we ignore higher-order diagrams. The full Standard Model Hamiltonian at tree level for the $pq \to p'q'$ process is given by [15]

$$\mathcal{H}_{\mathrm{SM}}^{\mathrm{tree}} = \frac{g_{EW}^2}{8} V_{pq}^* V_{p'q'} \Delta_{\mu\nu} (\bar{q}_\alpha p_\alpha)^\mu_{V-A} (\bar{q}'_\beta p'_\beta)^\nu_{V-A}, \tag{30}$$

where $g_{EW} \equiv g(\mu = m_W)$ is the $\mathrm{SU(2)_L}$ gauge coupling, α, β are $\mathrm{SU(3)_C}$ color indices, and the left- and right-handed weak currents are defined as

$$(\bar{q}p)_{V\pm A} = \bar{q}\gamma_\mu(1 \pm \gamma_5)p. \tag{31}$$

The propagator of the W boson is given by [4]

$$\Delta^{\mu\nu} = \frac{1}{k^2 - m_W^2}\left(g^{\mu\nu} - \frac{k^\mu k^\nu}{m_W^2}\right). \tag{32}$$

For $k^2 \ll m_W^2$, Eq. (32) reduces to [4]

$$\Delta^{\mu\nu}(k) \to \frac{g^{\mu\nu}}{m_W^2} + \mathcal{O}\left(\frac{k^2}{m_W^2}\right), \tag{33}$$

yielding a four-fermion interaction [4]:

$$\mathcal{H}_{\mathrm{SM}}^{\mathrm{tree}} = \frac{g_{EW}^2}{8m_W^2} V_{pq}^* V_{p'q'} (\bar{q}_\alpha p_\alpha)_{V-A} (\bar{q}'_\beta p'_\beta)_{V-A}. \tag{34}$$

Hence, from the matching condition $\mathcal{H}_{\mathrm{SM}}^{\mathrm{tree}} = \mathcal{H}_{\mathrm{eff}}$, we identify

$$\frac{G_F}{\sqrt{2}} \equiv \frac{g_{EW}^2}{8m_W^2}, \quad \mathcal{O}_2 \equiv (\bar{q}_\alpha p_\alpha)_{V-A} (\bar{q}'_\beta p'_\beta)_{V-A}, \quad C_2 = 1. \tag{35}$$

Thus, we have integrated out the W boson as a dynamical field, encoding its effect as a local four-point vertex in the effective Hamiltonian, as depicted in Fig. 7.

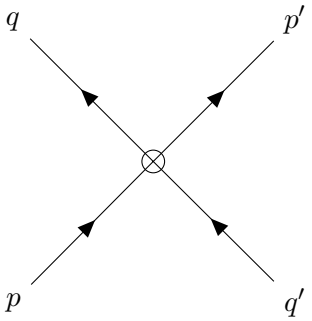

Figure 7: Effective four-fermion contact interaction of $pq \to p'q'$ after integrating out the W boson.

However, in reality, we have to include QCD corrections from gluon interactions [4]. Consequently, Wilson coefficients and operators run with μ after renormalization: $C_j = C_j(\mu)$, $\mathcal{O}_j = \mathcal{O}_j(\mu)$ [14]. The matrix elements $\langle f|\mathcal{O}_2(\mu)|i\rangle$ contain logarithms of the form $\log(\frac{m_b^2}{m_W^2})$ from gluon loop corrections, which are large at a high renormalization scale ($\mu = m_W$) [16]. Therefore, we evolve $C_j(\mu)$ and $\mathcal{O}_j(\mu)$ down to $\mu = m_b$ using renormalization-group equations (RGEs), which keep the amplitude μ-independent [16]. As a result, the large logarithms are resummed into the Wilson coefficients [4]. This RG evolution generates nonzero contributions to C_j beyond C_2, which is called operator mixing [4]. The hadronic matrix elements now describe the energy regime below $\mu = m_b$.

The contribution from other operators as a result of operator mixing can be understood as follows. With the inclusion of QCD corrections, gluon exchanges dress the four-fermion operator [14]. The one-loop Feynman diagrams are depicted in Fig. 8, where color indices are exchanged via the gluon.

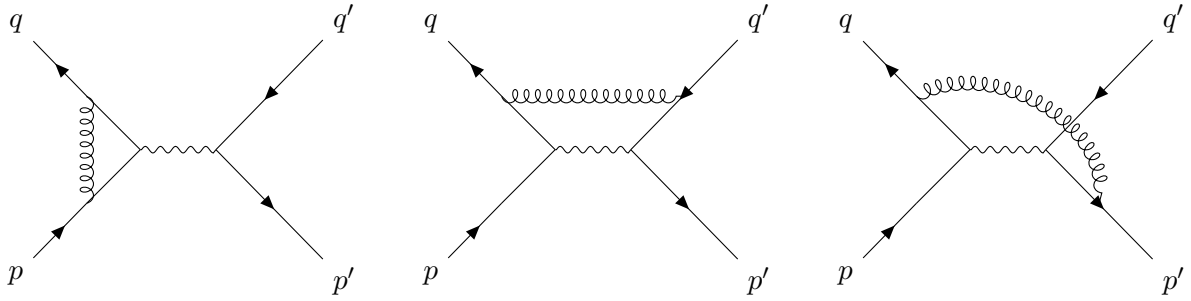

Figure 8: Leading-order QCD corrections to $pq \to p'q'$.

Each quark-gluon vertex introduces an additional color factor $T^a_{\alpha\beta}$ that multiplies the amplitude, allowing for the exchange of color indices. Using the $\mathrm{SU}(3)_\mathrm{C}$ identity [4],

$$T^a_{\alpha\beta}T^a_{\gamma\delta} = \frac{1}{2}\left(\delta_{\alpha\delta}\delta_{\beta\gamma} - \frac{\delta_{\alpha\beta}\delta_{\gamma\delta}}{N_c}\right), \tag{36}$$

the middle and right-most diagrams yield the following color contractions:

$$T^a_{\alpha\beta}T^a_{\gamma\delta}(\bar{q}_\alpha p_\beta)_{V-A}(\bar{q}'_\gamma p'_\delta)_{V-A} = \frac{1}{2}(\bar{q}_\alpha p_\beta)_{V-A}(\bar{q}'_\beta p'_\alpha)_{V-A} - \frac{1}{2N_c}(\bar{q}_\alpha p_\alpha)_{V-A}(\bar{q}'_\beta p'_\beta)_{V-A}, \tag{37}$$

with $N_c = 3$ for $\mathrm{SU(3)_C}$.

Hence, we see that QCD corrections give rise to a new operator with mixed color indices, namely [4]

$$\mathcal{O}_1 \equiv (\bar{q}_\alpha p_\beta)_{V-A}(\bar{q}'_\beta p'_\alpha)_{V-A}, \tag{38}$$

with nonzero contributions to its coefficient C_1, while slightly modifying C_2.

For the left diagram, the gluon only couples within the same current and consequently only renormalizes $\mathcal{O}_2$:

$$T^a_{\alpha\delta} T^a_{\delta\gamma} (\bar{q}_\alpha p_\gamma)_{V-A}(\bar{q}'_\beta p'_\beta)_{V-A} = \frac{1}{2}\left(\frac{N_c^2 - 1}{N_c}\right)(\bar{q}_\alpha p_\alpha)_{V-A}(\bar{q}'_\beta p'_\beta)_{V-A}. \tag{39}$$

Consequently, the resulting low-energy effective Hamiltonian at $\mu = m_b$ with only one-loop QCD corrections becomes

$$\mathcal{H}_{\text{eff}}(\mu = m_b) = \frac{G_F}{\sqrt{2}} V^*_{pq} V_{p'q'} \left(C_1 \mathcal{O}_1 + C_2 \mathcal{O}_2\right), \tag{40}$$

with $C_1 \ll C_2$ [4].

4.2 Factorization

Next, we evaluate the hadronic matrix elements in the effective Hamiltonian at $\mu = m_b$ for the color-allowed and color-suppressed tree topologies of the decay $B_q \to M_1 M_2$, where

$$|B_q\rangle = |\bar{b}q\rangle, \quad |M_1\rangle = |\bar{q}_1 q\rangle, \quad |M_2\rangle = |\bar{q}_3 q_2\rangle, \tag{41}$$

as illustrated in Figs. 3a and 3b. We only include contributions from first-order QCD corrections. Thus, the amplitude only receives contributions from $\mathcal{O}_1$ and $\mathcal{O}_2$.

4.2.1 Color-Allowed Tree Topology

For the color-allowed tree topology (Fig. 3a), we obtain the following relation for the color-allowed (CA) amplitude A_{CA}:

$$A_{\text{CA}} \sim C_1(\mu)\langle M_1 M_2|\mathcal{O}_1(\mu)|B\rangle + C_2(\mu)\langle M_1 M_2|\mathcal{O}_2(\mu)|B\rangle. \tag{42}$$

First, we focus on the matrix element $\langle M_1 M_2|\mathcal{O}_2(\mu)|B\rangle$. This matrix element encodes long-distance QCD dynamics for which an exact calculation from first principles is not yet possible, as this has to be treated non-perturbatively [17]. The most common approach to approximate such matrix elements is the factorization approximation, where we assume that the two hadronization processes occur independently: the transition $B \to M_1$, parametrized by the form factor $f_{B\to M_1}$, and the creation of the M_2 meson from the vacuum, parametrized by the decay constant f_{M_2} [4], which is independent of the decay mode [4]. The resulting matrix element is given by [4]

$$\langle M_1 M_2|\mathcal{O}_2(\mu)|B\rangle\big|_{\text{fact}} = \langle M_2|(\bar{q}_3 q_2)_{V-A}|0\rangle\langle M_1|(\bar{q}_1 b)_{V-A}|B\rangle \sim f_{M_2} f_{B\to M_1}. \tag{43}$$

Although the four-quark matrix element $\langle M_1 M_2|(\bar{q}_3 q_2)_{V-A}(\bar{q}_1 b)_{V-A}|B\rangle$ carries a renormalization scale dependence, the factorized current matrix elements are μ-independent [16].

Consequently, the μ-dependence of the Wilson coefficients is left uncanceled in naive factorization [16]. Non-factorizable contributions are therefore needed to recover the scale dependence of the full hadronic matrix element, so that the physical amplitude remains independent of the renormalization scale [4], [16]. These effects will be discussed at the end of this section in more detail.

The operator $\mathcal{O}_1$ consists of a mixed color structure. However, in the color-allowed tree topology, only the color-singlet current contributes. Thus, we decompose the operator $\mathcal{O}_1$ into a color-singlet and a color-octet part through a Fierz reordering [18]:

$$\mathcal{O}_1 = (\bar{q}_3^\alpha q_2^\beta)_{V-A}(\bar{q}_1^\beta b^\alpha)_{V-A} = (\bar{q}_3^\alpha q_2^\beta)_{V-A}(\bar{q}_1^\gamma b^\delta)_{V-A}\delta_{\alpha\delta}\delta_{\beta\gamma}. \tag{44}$$

Using Eq. (36), we can rewrite the factor $\delta_{\alpha\delta}\delta_{\beta\gamma}$ as

$$\delta_{\alpha\delta}\delta_{\beta\gamma} = \frac{1}{N_c}\delta_{\alpha\beta}\delta_{\gamma\delta} + 2T^a_{\alpha\beta}T^a_{\gamma\delta}. \tag{45}$$

This gives

$$\mathcal{O}_1 = \frac{1}{N_c}\mathcal{O}_2 + 2\tilde{\mathcal{O}}_{\mathrm{CA}}, \tag{46}$$

where $\tilde{\mathcal{O}}_{\mathrm{CA}}$ is the product of two color-octet currents, given by

$$\tilde{\mathcal{O}}_{\mathrm{CA}} \equiv T^a_{\alpha\beta}(\bar{q}_3^\alpha q_2^\beta)_{V-A}T^a_{\gamma\delta}(\bar{q}_1^\gamma b^\delta)_{V-A}. \tag{47}$$

We disregard the color-octet term $\tilde{\mathcal{O}}_{\mathrm{CA}}$ in naive factorization, since matrix elements of octet currents between color-singlet states vanish [18], [19]. Hence, we have

$$A^{\mathrm{CA}}_{\mathrm{tree}} \sim a_1\langle M_1M_2|\mathcal{O}_2|B\rangle \sim a_1 f_{M_2} f_{B\to M_1}, \tag{48}$$

where the effective coefficient a_1 is defined as [20]

$$a_1 \equiv C_2 + \frac{C_1}{N_c}. \tag{49}$$

We now turn to the calculation of the form factor $f_{B\to M_1}$ and restrict our discussion to color-allowed $B \to PV$ decays, where $M_1 = P = |\bar{q}_1 q\rangle$ denotes a pseudoscalar meson and $M_2 = V = |\bar{q}_3 q_2\rangle$ denotes a vector meson. An example is the decay $B^0_d \to D^-\rho^+$. This setup allows us to draw a parallel with the modes $B^+ \to J/\psi\pi^+$ and $B^+ \to J/\psi K^+$, which are also $B \to PV$ decays, although they proceed through a color-suppressed tree topology, as will be discussed in Section 4.2.2.

The matrix element factorizes as

$$\langle PV|\mathcal{O}_2|B\rangle|_{\mathrm{fact}} = \langle V|(\bar{q}_3 q_2)_{V-A}|0\rangle\langle P|(\bar{q}_1 b)_{V-A}|B\rangle. \tag{50}$$

The first factor defines the decay constant f_V of the vector meson [4], [21]:

$$\langle V|(\bar{q}_3 q_2)_{V\mp A}|0\rangle = \langle V(p_V,\epsilon)|\bar{q}_3\gamma_\mu q_2|0\rangle \equiv f_V m_V \epsilon^*_\mu, \tag{51}$$

where m_V is the mass of the vector meson and ϵ_μ its polarization four-vector. The second factor, describing the $B \to P$ transition, is parametrized by the form factors $f^+_{B\to P}$ and $f^0_{B\to P}$ as [4], [21]

$$\begin{aligned}\langle P(p_P)|(\bar{q}_1 b)_{V\mp A}|B(p_B)\rangle = &\left[(p_B+p_P)_\mu - \frac{m_B^2-m_P^2}{q^2}q_\mu\right] f^+_{B\to P}(q^2) \\ &+ \left[\frac{m_B^2-m_P^2}{q^2}q_\mu\right] f^0_{B\to P}(q^2),\end{aligned} \tag{52}$$

with $q^\mu \equiv p_B^\mu - p_P^\mu = p_V^\mu$ and $q^2 = m_V^2$.

The polarization and momentum four-vectors for vector mesons satisfy the transversality condition

$$\epsilon_\mu p^\mu = \epsilon^*_\mu p^\mu = 0. \tag{53}$$

Consequently, only the term proportional to $f^+_{B\to P}$ contributes, resulting in

$$\langle PV|\mathcal{O}_2|B\rangle|_{\text{fact}} = f_V m_V \epsilon^*_\mu (p_B+p_P)^\mu f^+_{B\to P}(q^2). \tag{54}$$

In color-allowed tree topologies, factorization is expected to work especially well for heavy-light final states, where the spectator quark becomes part of a heavy meson M_1 containing a charm (anti)quark, while the emitted meson M_2 is light [4]. The decay $B^0_d \to D^-\rho^+$ is an example of such a process. Here, the energetic ρ^+ meson quickly separates from the D^- meson, suppressing long-distance strong interactions between the two final-state mesons. Meanwhile, the charm quark forming the D^- is comparatively slow, so it can combine more easily with the spectator quark. This makes non-factorizable corrections to the hadronic matrix elements expected to be relatively small in this type of decay [4].

This is not the case for decays where both mesons are light, such as $B_d^0 \to \pi^+\rho^-$. The $\bar{q}_1$ quark of the M_1 meson moves with a large velocity relative to the spectator quark q, which complicates hadronization [4]. Hence, for the hadronization of M_1, additional virtual gluon exchanges become more important. These corrections can appear as vertex corrections, spectator-scattering contributions involving the spectator quark, and long-distance final-state rescattering between the outgoing mesons [4], [22], [23]. Consequently, non-factorizable corrections are expected to be larger than in color-allowed heavy-light decays.

4.2.2 Color-Suppressed Tree Topology

$B \to PV$ decays can also proceed through a color-suppressed tree topology, where we take $M_1 = P = |\bar{q}_1 q\rangle$ and $M_2 = V = |\bar{q}_3 q_2\rangle$ (see Fig. 3b). As mentioned in the previous subsection, this topology is the one relevant for the $B^+ \to J/\psi\pi^+$ and $B^+ \to J/\psi K^+$ modes. In contrast to the color-allowed case, the naive factorization picture is less straightforward here. From Fig. 3b, the weak interaction can be split up into a $\bar{b} \to \bar{q}_3$ transition and a $\bar{q}_1 q_2$ pair created from the vacuum. However, these do not correspond to a well-defined form factor and decay constant, since q_2 and $\bar{q}_1$ end up in different final-state mesons. As a consequence, the amplitude cannot be reliably factorized in the naive factorization picture, since the two hadronization processes that form M_1 and M_2 are not cleanly separable.

Nevertheless, factorization is still applied as an approximation by assuming that the color-suppressed tree amplitude can be written analogously to the color-allowed case. In this picture, the $\bar{b} \to \bar{q}_1$ transition forming the pseudoscalar meson M_1 is parametrized by the form factor $f^+_{B\to P}$, while the creation of the $\bar{q}_3 q_2$ pair forming the vector meson M_2 is described by the decay constant f_V. Since the color flow is crossed in this case, the operator $\mathcal{O}_2$ has to be rewritten accordingly:

$$\mathcal{O}_2 = (\bar{q}_3^\alpha q_2^\alpha)_{V-A}(\bar{q}_1^\beta b^\beta)_{V-A} = (\bar{q}_3^\alpha q_2^\delta)_{V-A}(\bar{q}_1^\beta b^\gamma)_{V-A}\delta_{\alpha\delta}\delta_{\beta\gamma}. \tag{55}$$

Using Eq. (45), this becomes

$$\mathcal{O}_2 = \frac{1}{N_c}\mathcal{O}_1 + \tilde{\mathcal{O}}_{\text{CS}}, \tag{56}$$

where

$$\tilde{\mathcal{O}}_{\text{CS}} \equiv 2T^a_{\alpha\beta}T^a_{\gamma\delta}(\bar{q}_3^\alpha q_2^\delta)_{V-A}(\bar{q}_1^\beta b^\gamma)_{V-A}. \tag{57}$$

Again, we disregard the color-octet term $\tilde{\mathcal{O}}_{\text{CS}}$ in naive factorization. This yields the following expression for the amplitude:

$$A^{\text{tree}}_{\text{CS}} \sim a_2\langle PV|\mathcal{O}_1|B\rangle \sim a_2 f_V f^+_{B\to P}, \tag{58}$$

where the effective coefficient a_2 is defined as [20]

$$a_2 \equiv C_1 + \frac{C_2}{N_c}. \tag{59}$$

For non-leptonic B-meson decays, $C_1 = \mathcal{O}(10^{-1})$ and $C_2 = \mathcal{O}(1)$ [4]. If QCD corrections are neglected and one sets $C_1 = 0$, one finds

$$\frac{A^{\text{tree}}_{\text{CS}}}{A^{\text{tree}}_{\text{CA}}} = \frac{1}{N_c}, \tag{60}$$

in agreement with the discussion in Section 2.

Since the naive factorization picture does not hold exactly for the color-suppressed topology, non-factorizable contributions are expected to play an important role. Consequently, naive factorization is generally less reliable for color-suppressed amplitudes [24].

4.3 Full Effective Hamiltonian for $|\Delta B|= 1$, $\Delta C = 0$ Decays

We now derive the full effective Hamiltonian for $|\Delta B|= 1$, $\Delta C = 0$ decays, where ΔB and ΔC denote the changes in bottomness and charm quantum number, respectively, between the initial and final state. This sector covers the decay modes considered in the global fit, as shown in Fig. 4. In addition to the leading tree topologies and the first-order QCD corrections discussed above, we now also include penguin contributions. The color-allowed and color-suppressed penguin topologies are depicted in Figs. 3c and 3d, respectively.

Since the virtual gluon in the color-suppressed penguin topology can also be replaced by a color singlet (i.e. a photon or Z boson), penguin topologies can be further divided into gluonic and electroweak penguins [14].

For such decays, the operators corresponding to gluonic penguin topologies are [14]

$$\mathcal{O}_3 = (\bar{r}_\alpha b_\alpha)_{V-A} \sum_q (\bar{q}_\beta q_\beta)_{V-A}, \quad \mathcal{O}_4 = (\bar{r}_\alpha b_\beta)_{V-A} \sum_q (\bar{q}_\beta q_\alpha)_{V-A}, \tag{61}$$

$$\mathcal{O}_5 = (\bar{r}_\alpha b_\alpha)_{V-A} \sum_q (\bar{q}_\beta q_\beta)_{V+A}, \quad \mathcal{O}_6 = (\bar{r}_\alpha b_\beta)_{V-A} \sum_q (\bar{q}_\beta q_\alpha)_{V+A}, \tag{62}$$

where $q \in \{u, c, d, s\}$ and $r \in \{d, s\}$. Mixed-color structures arise from additional gluon exchanges. Mixed-chiral structures of $\mathcal{O}_5$ and $\mathcal{O}_6$ reflect the fact that the strong interaction is chirality-blind.

The operators corresponding to electroweak penguin topologies are [4]

$$\mathcal{O}_7 = \frac{3}{2}(\bar{r}_\alpha b_\alpha)_{V-A} \sum_q e_q \, (\bar{q}_\beta q_\beta)_{V+A}, \qquad \mathcal{O}_8 = \frac{3}{2}(\bar{r}_\alpha b_\beta)_{V-A} \sum_q e_q \, (\bar{q}_\beta q_\alpha)_{V+A}, \tag{63}$$

$$\mathcal{O}_9 = \frac{3}{2}(\bar{r}_\alpha b_\alpha)_{V-A} \sum_q e_q \, (\bar{q}_\beta q_\beta)_{V-A}, \qquad \mathcal{O}_{10} = \frac{3}{2}(\bar{r}_\alpha b_\beta)_{V-A} \sum_q e_q \, (\bar{q}_\beta q_\alpha)_{V-A}, \tag{64}$$

where e_q denotes the charge of quark q. This additional factor is due to the photon coupling differently to quarks depending on their charge. The Z boson is integrated out along with the W boson, with its effects encoded in the Wilson coefficients. The factor $\frac{3}{2}$ is a conventional normalization factor, such that $\frac{3}{2}e_q = 1$ if q is an up-type quark. The photon, similarly to the gluon, is chirality-blind, allowing mixed chiral structures.

Finally, with the top quark integrated out, the effective Hamiltonian is given by [4], [14]

$$\mathcal{H}_{\text{eff}} = \frac{G_F}{\sqrt{2}} \sum_{j=u,c} V_{jr}^* V_{jb} \left[\sum_{k=1}^{2} C_k(\mu) \mathcal{O}_k^j(\mu) + \sum_{k=3}^{10} C_k(\mu) \mathcal{O}_k(\mu) \right] + \text{h.c.}, \tag{65}$$

where [4], [14]

$$\mathcal{O}_1^j = (\bar{r}_\alpha j_\beta)_{V-A} (\bar{j}_\beta b_\alpha)_{V-A}, \quad \mathcal{O}_2^j = (\bar{r}_\alpha j_\alpha)_{V-A} (\bar{j}_\beta b_\beta)_{V-A}. \tag{66}$$

Importantly, since the penguin operators are also four-quark operators, their matrix elements can be treated analogously in naive factorization, where they are factorized into products of decay constants and form factors [25].

5 Branching Fraction Ratios

Besides the CP asymmetries introduced in Section 3, branching fraction ratios provide a complementary class of observables that can be incorporated into the global fit. Such ratios are available for many decay modes and can therefore be valuable additional inputs. In particular, the experimentally measured ratio of CP-averaged branching fractions, $\overline{\mathcal{B}}(B^\pm \to J/\psi\pi^\pm)/\overline{\mathcal{B}}(B^\pm \to J/\psi K^\pm)$, provides an additional constraint on the hadronic parameters of the B^+ modes.

5.1 General Relations for Two-Body Decays

For a decay $X \to f$, with partial decay rate $\Gamma(X \to f)$ and total decay rate $\Gamma_{\rm tot}$, the branching fraction is defined as

$$\mathcal{B}(X \to f) \equiv \frac{\Gamma(X \to f)}{\Gamma_{\rm tot}}. \tag{67}$$

For a particle X decaying into two particles with four-momenta p_1 and p_2, the decay rate can be evaluated in the rest frame of X. Since Γ is Lorentz invariant, this gives a general result. From the derivation given in Appendix A, one obtains [13]

$$\Gamma = \frac{1}{32\pi^2}\int |A|^2 \frac{|\vec{p}|}{M^2} d\Omega, \tag{68}$$

where A is the decay amplitude, M is the mass of the decaying particle, and $|\vec{p}| \equiv |\vec{p}_1| = |\vec{p}_2|$ is the magnitude of the three-momentum of either final-state particle, given by [13]

$$|\vec{p}| = \frac{1}{2M}\sqrt{\lambda(M^2, m_1^2, m_2^2)}, \tag{69}$$

where the Källén function is defined as [13]

$$\lambda(a, b, c) \equiv a^2 + b^2 + c^2 - 2ab - 2ac - 2bc. \tag{70}$$

For an isotropic decay, the angular integration yields

$$\Gamma = \frac{1}{8\pi}|A|^2 \frac{|\vec{p}_1|}{M^2}. \tag{71}$$

For two-body decays $X \to f_1^X f_2^X$ and $Y \to f_1^Y f_2^Y$, the branching fraction ratio is then

$$\mathcal{R} \equiv \frac{\mathcal{B}\left(X \to f_1^X f_2^X\right)}{\mathcal{B}\left(Y \to f_1^Y f_2^Y\right)} = \left|\frac{A_X}{A_Y}\right|^2 \frac{|\vec{p}_X|}{|\vec{p}_Y|}\left(\frac{M_Y}{M_X}\right)^2 \frac{\tau_X}{\tau_Y}. \tag{72}$$

5.2 Application to $B^+ \to J/\psi\pi^+$ and $B^+ \to J/\psi K^+$

We now apply the general expression in Eq. (72) to the decays $B^+ \to J/\psi\pi^+$ and $B^+ \to J/\psi K^+$.

Since the experimentally measured branching fractions are CP-averaged, we define

$$\overline{\mathcal{B}}\left(B^\pm \to f^\pm\right) \equiv \frac{1}{2}\left[\mathcal{B}\left(B^+ \to f^+\right) + \mathcal{B}\left(B^- \to f^-\right)\right]. \tag{73}$$

The corresponding ratio of CP-averaged branching fractions is then

$$\overline{\mathcal{R}} \equiv \frac{\overline{\mathcal{B}}\left(B^\pm \to J/\psi\pi^\pm\right)}{\overline{\mathcal{B}}\left(B^\pm \to J/\psi K^\pm\right)} = \frac{\left|A(B^+ \to J/\psi\pi^+)\right|^2 + \left|A(B^- \to J/\psi\pi^-)\right|^2}{\left|A(B^+ \to J/\psi K^+)\right|^2 + \left|A(B^- \to J/\psi K^-)\right|^2}\frac{|\vec{p}_{\pi^+}|}{|\vec{p}_{K^+}|}. \tag{74}$$

Using Eq. (69), we obtain

$$\frac{|\vec{p}_{\pi^+}|}{|\vec{p}_{K^+}|} = \frac{\sqrt{\lambda\left(m_{B^+}^2, m_{J/\psi}^2, m_{\pi^+}^2\right)}}{\sqrt{\lambda\left(m_{B^+}^2, m_{J/\psi}^2, m_{K^+}^2\right)}} \simeq 1.02614825(228), \tag{75}$$

using masses from the PDG [13].

Substituting Eqs. (12) and (19), together with their CP-conjugate amplitudes obtained by replacing $\gamma \to -\gamma$, into Eq. (74), the ratio of CP-averaged branching fractions can be written as

$$\overline{\mathcal{R}} = \epsilon\,\xi\, f(a_{\rm sca}, \theta_{\rm sca}, x, \sigma, a'_{\rm sca}, \theta'_{\rm sca}, x', \sigma')\frac{|\vec{p}_{\pi^+}|}{|\vec{p}_{K^+}|}, \tag{76}$$

where

$$f \equiv \frac{1 - 2\cos\gamma\,(a_{\rm sca}\cos\theta_{\rm sca} + x\cos\sigma) + 2a_{\rm sca}x\cos(\theta_{\rm sca} - \sigma) + a_{\rm sca}^2 + x^2}{1 + 2\epsilon\cos\gamma\left(a'_{\rm sca}\cos\theta'_{\rm sca} + x'\cos\sigma'\right) + \epsilon^2\left(2a'_{\rm sca}x'\cos(\theta'_{\rm sca} - \sigma') + {a'_{\rm sca}}^2 + x'^2\right)}. \tag{77}$$

The function $f(a_{\rm sca}, \theta_{\rm sca}, x, \sigma, a'_{\rm sca}, \theta'_{\rm sca}, x', \sigma')$ collects the dependence on the penguin and annihilation parameters. Here, the unprimed quantities refer to $B^\pm \to J/\psi\pi^\pm$, while the primed quantities correspond to $B^\pm \to J/\psi K^\pm$.

The factor ξ contains the ratio of hadronic amplitudes associated with these two decay modes:

$$\xi \equiv \left|\frac{T + P^{(c)} - P^{(t)}}{T' + P'^{(c)} - P'^{(t)}}\right|^2 = \left|\frac{T}{T'}\right|^2 \left|\frac{1 + \frac{P^{(c)} - P^{(t)}}{T}}{1 + \frac{P'^{(c)} - P'^{(t)}}{T'}}\right|^2. \tag{78}$$

5.2.1 U-spin Breaking in ξ

Since ξ is a ratio of hadronic amplitudes associated with two different decay modes, the corresponding form factors and decay constants do not cancel. Consequently, ξ can receive both factorizable and non-factorizable U-spin-breaking corrections.

This is different for the penguin parameters defined for the $B^+ \to J/\psi\pi^+$ and $B^+ \to J/\psi K^+$ modes in Eqs. (15) and (23), respectively, as well as for the corresponding annihilation parameters introduced in Eqs. (16) and (24). These quantities are defined as ratios of hadronic

amplitudes contributing to the same decay mode. Consequently, in the factorization approach, the corresponding decay constants and form factors cancel, implying the cancellation of factorizable U-spin-breaking effects [26]. This justifies the use of the U-spin relation given in Eq. (26).

5.2.2 Benchmark Scenarios for ξ

To estimate ξ, we therefore distinguish between three scenarios: (i) the exact U-spin limit, (ii) the case where only factorizable symmetry-breaking effects are included, and (iii) the case where additional non-factorizable symmetry-breaking effects are taken into account.

Exact U-spin symmetry In the limit of exact U-spin symmetry, i.e. in the absence of both factorizable and non-factorizable symmetry breaking, Eq. (78) becomes

$$\xi^{\text{U-spin}} = 1. \tag{79}$$

Factorizable symmetry breaking In the factorization approach, Eq. (78) becomes

$$\xi^{\text{fact}} = \left|\frac{T}{T'}\right|^2_{\text{fact}} \left|\frac{1+\frac{P^{(c)}-P^{(t)}}{T}}{1+\frac{P'^{(c)}-P'^{(t)}}{T'}}\right|^2_{\text{fact}}. \tag{80}$$

The penguin-to-tree factors in Eq. (80) involve ratios of amplitudes contributing to the same decay mode. In the factorization approach, the common hadronic factors, namely the decay constants and form factors, therefore cancel in these ratios [26]. Moreover, both the unprimed and primed modes are described by the same $|\Delta B|= 1$, $\Delta C = 0$ effective weak Hamiltonian of Eq. (65), so that the short-distance ratio of Wilson coefficients remains the same for the two modes. Consequently, we have

$$\left.\frac{P^{(c)} - P^{(t)}}{T}\right|_{\text{fact}} = \left.\frac{P'^{(c)} - P'^{(t)}}{T'}\right|_{\text{fact}}. \tag{81}$$

Equation (80) then reduces to

$$\xi^{\text{fact}} = \left|\frac{T}{T'}\right|^2_{\text{fact}}. \tag{82}$$

We now calculate $\left|T/T'\right|^2_{\text{fact}}$ in the factorization approach. The decays $B^+ \to J/\psi\pi^+$ and $B^+ \to J/\psi K^+$ are treated as $B \to P^{(\prime)}V$ decays dominated at leading order by a color-suppressed tree topology, shown in Fig. 3b. Here, $V = J/\psi$, $P = \pi^+$ and $P' = K^+$. From Section 4.2.2, the factorized tree amplitude is

$$\begin{aligned} A_{\text{tree}}(B \to P^{(\prime)}V)\Big|_{\text{fact}} &= \frac{G_F}{\sqrt{2}} V^*_{cb}V_{cq}a_2 f_V m_V \epsilon^{(\prime)*}_\mu (p_B + p_{P^{(\prime)}})^\mu f^+_{B\to P^{(\prime)}}(q^2) \\ &= V^*_{cb}V_{cq}\, T^{(\prime)}\Big|_{\text{fact}}, \end{aligned} \tag{83}$$

where $q = d$ for the unprimed case and $q = s$ for the primed case. In the form factor, q^2 denotes the momentum transfer squared, which is given by $q^2 = m^2_{J/\psi}$ for both decay modes.

In the convention used here, the momentum-polarization contraction $\epsilon_\mu^{(\prime)*}(p_B + p_{P^{(\prime)}})^\mu$ is included in the definition of the amplitudes. These amplitudes therefore correspond to full amplitudes rather than reduced scalar amplitudes.

Hence, Eq. (82) becomes

$$\xi^{\text{fact}} = \left| \frac{\epsilon_\mu^*(p_B + p_P)^\mu f_{B\to P}^+(q^2)}{\epsilon_\mu'^*(p_B + p_{P'})^\mu f_{B\to P'}^+(q^2)} \right|^2 = \left[\frac{|\vec{p}_P|}{|\vec{p}_{P'}|} \frac{f_{B\to P}^+(m_{J/\psi}^2)}{f_{B\to P'}^+(m_{J/\psi}^2)} \right]^2 . \tag{84}$$

In the last step, we used

$$\left| \frac{\epsilon_\mu^*(p_B + p_P)^\mu}{\epsilon_\mu'^*(p_B + p_{P'})^\mu} \right| = \frac{|\vec{p}_P|}{|\vec{p}_{P'}|}. \tag{85}$$

This relation is derived in Appendix B, where it is shown that the transverse polarization contractions vanish and only the longitudinal polarization contributes.

For the $B \to K$ form factor, we use

$$f_{B\to K}^+(m_{J/\psi}^2) = 0.613 \pm 0.018. \tag{86}$$

This value was determined by the HPQCD collaboration [27], which calculated the $B \to K$ form factors from lattice QCD simulations of the $B \to K\ell^+\ell^-$ decay. The form factor was interpolated to $q^2 = m_{J/\psi}^2$ using the accompanying Python script provided by the authors [27]. For the spectator-quark mass, we use the average of the up- and down-quark masses. Isospin-breaking effects were found to be negligible.

For the $B \to \pi$ form factor, we use

$$f_{B\to\pi}^+(m_{J/\psi}^2) = 0.4106 \pm 0.0256. \tag{87}$$

This value is based on the recent analysis by Cui et al. [28], who used QCD light-cone sum rules combined with soft-collinear effective theory constraints. The value was obtained by evaluating their fitted parametrization at $q^2 = m_{J/\psi}^2$, using the Python script described in Appendix C. Their analysis is performed in the isospin-symmetric limit. The result is consistent with the independent JLQCD determination [29], which yielded $f_{B\to\pi}^+(m_{J/\psi}^2) = 0.4114 \pm 0.0535$.

Substituting these inputs into Eq. (84), we obtain

$$\xi^{\text{fact}} = 0.47 \pm 0.07. \tag{88}$$

It should be noted that ξ^{fact} is a squared-amplitude quantity. At amplitude level, the result in Eq. (88) therefore corresponds to a factorizable symmetry breaking of $(31 \pm 5)\%$.

Non-factorizable symmetry breaking Beyond the factorization approximation, additional non-factorizable symmetry-breaking effects may modify both ξ and the assumed U-spin relation in Eq. (26) for the penguin and annihilation parameters. Since $\overline{\mathcal{R}}$ is experimentally accessible, it can be used as a probe of the overall size of such effects.

In the exact U-spin limit for ξ, the branching fraction ratio takes the form

$$\overline{\mathcal{R}}|_{U\text{-spin}} = \epsilon\, f(a_{\rm sca}, \theta_{\rm sca}, x, \sigma)\, \frac{|\vec{p}_{\pi^+}|}{|\vec{p}_{K^+}|}. \tag{89}$$

Similarly, in the factorization approximation the U-spin relation given in Eq. (26) is exact, following the same reasoning as in the previous subsection. Accordingly, the branching fraction ratio in the factorization approximation becomes

$$\overline{\mathcal{R}}|_{\rm fact} = \epsilon\, \xi^{\rm fact}\, f(a_{\rm sca}, \theta_{\rm sca}, x, \sigma)\, \frac{|\vec{p}_{\pi^+}|}{|\vec{p}_{K^+}|}. \tag{90}$$

To account for possible additional non-factorizable symmetry-breaking effects, we write

$$\overline{\mathcal{R}} = \epsilon\, \xi^{\mathcal{R}}\, f(a_{\rm sca}, \theta_{\rm sca}, x, \sigma)\, \frac{|\vec{p}_{\pi^+}|}{|\vec{p}_{K^+}|}, \tag{91}$$

with

$$\xi^{\mathcal{R}} \equiv \kappa\, \xi^{\rm fact}, \tag{92}$$

where κ is an effective correction factor parametrizing non-factorizable symmetry-breaking effects entering both ξ and the assumed U-spin relation for the penguin and annihilation parameters.

In the factorization limit, one has

$$\kappa \to \kappa^{\rm fact} = 1, \tag{93}$$

so that

$$\xi^{\mathcal{R}} \to \xi^{\rm fact}. \tag{94}$$

In the limit that non-factorizable symmetry breaking in the assumed U-spin relation is negligible, one has

$$\xi^{\mathcal{R}} \to \xi. \tag{95}$$

5.2.3 Ratio of Direct CP Asymmetries

In principle, we can also probe ξ by using the experimental information on the ratio of direct CP asymmetries. This follows from combining Eq. (76) with the expressions for the direct CP asymmetries in Eqs. (18) and (25), which gives

$$\frac{\mathcal{A}_{\rm CP}^{\rm dir}(B^+ \to J/\psi\pi^+)}{\mathcal{A}_{\rm CP}^{\rm dir}(B^+ \to J/\psi K^+)} = -\frac{\xi}{\overline{\mathcal{R}}}\, \frac{|\vec{p}_{\pi^+}|}{|\vec{p}_{K^+}|}\, \frac{a_{\rm sca} \sin\theta_{\rm sca} + x \sin\sigma}{a'_{\rm sca} \sin\theta'_{\rm sca} + x' \sin\sigma'}. \tag{96}$$

Under the U-spin relation given by Eq. (26), the ratio of the sine combinations reduces to unity. Using the experimental measurements for the direct CP asymmetries and $\overline{\mathcal{R}}$ given in Section 6.4, this relation gives

$$\xi|_{\text{U-spin}} = -0.31 \pm 0.53. \tag{97}$$

The large uncertainty means that the 68% confidence interval still includes positive values of ξ. However, the negative central value is not physically consistent with the definition of ξ, since ξ is a squared ratio of hadronic amplitudes and must therefore satisfy $\xi \geq 0$, as shown in Eq. (78). The negative central value arises from the current experimental central values of the direct CP asymmetries. In particular, the measurement of $\mathcal{A}_{\mathrm{CP}}^{\mathrm{dir}}(B^+ \to J/\psi K^+)$ has limited precision and is compatible with both signs within 1σ, while its central value is positive (see Eq. (99)). However, under the U-spin relation in Eq. (26), the direct CP asymmetries of $B^+ \to J/\psi\pi^+$ and $B^+ \to J/\psi K^+$ are expected to have opposite signs.

This shows that, with the current experimental precision, it is difficult to externally constrain ξ directly from the ratio of direct CP asymmetries. Instead, information on ξ can be obtained more reliably within a global fit, where the experimental measurements of the direct CP asymmetries and $\overline{\mathcal{R}}$ are included as separate inputs. The methodology of this fit is described in the next section.

6 Methodology

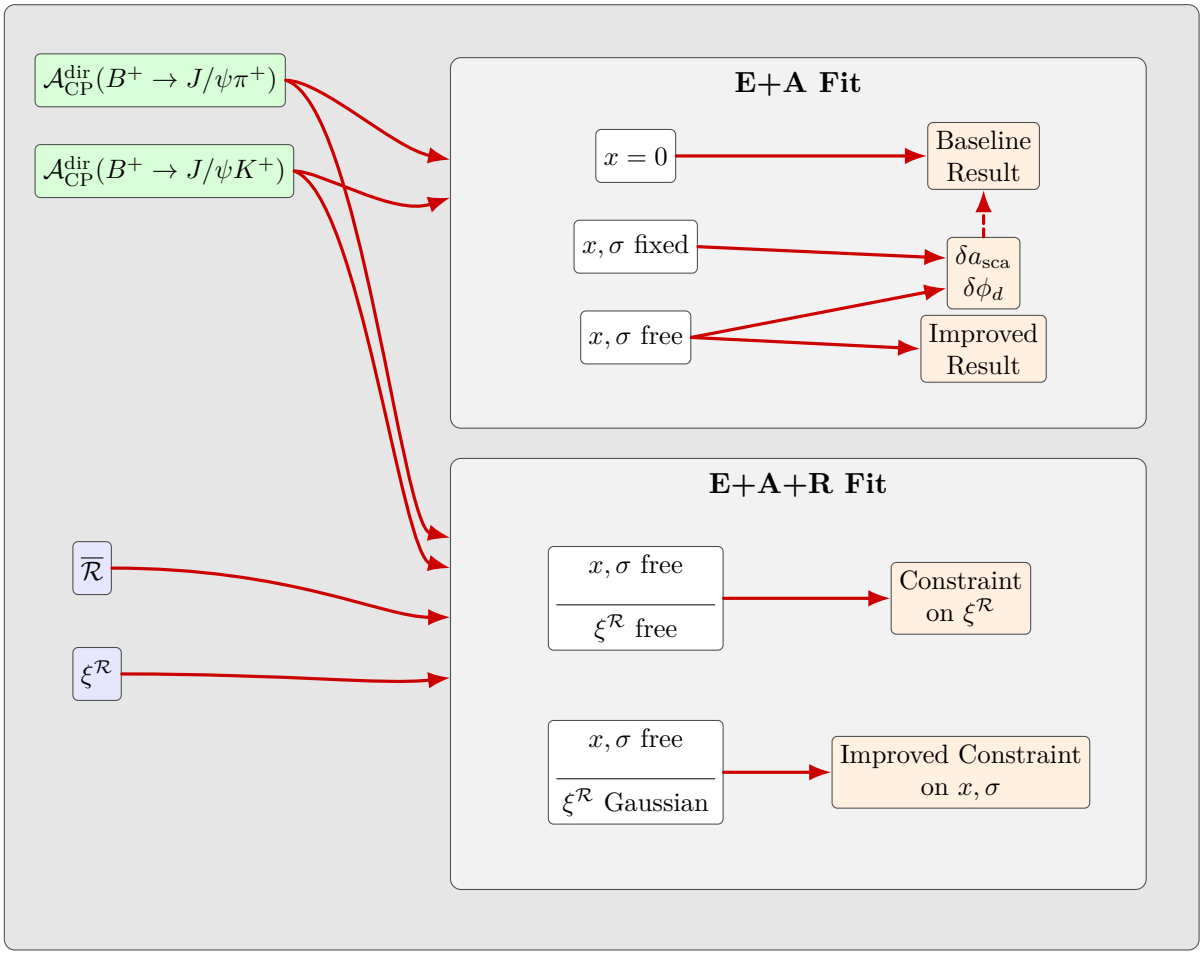

Figure 9: Schematic overview of the Extended + Annihilation (E+A) and Extended + Annihilation + Ratio (E+A+R) fit strategies considered in this work. The E+A Fit with $x = 0$ defines the baseline strategy (i.e. the Extended Fit), which is subsequently generalized by including the annihilation parameters (x, σ).

We extend the fitting strategy of Ref. [5], shown in Fig. 4, by including the annihilation parameters (x, σ) in the parametrization of the observables. The resulting fit strategies developed in this thesis are schematically summarized in Fig. 9. The combiner module used to perform these fits in `GammaCombo` is provided in Appendix D.

6.1 E+A Fit

We denote the Extended Fit supplemented by the reparametrized expressions for the B^+ modes in terms of x and σ as the *Extended + Annihilation* (E+A) Fit. To probe the sensitivity to annihilation contributions in a controlled way, we focus on annihilation topologies in isolation and therefore neglect exchange and penguin-annihilation topologies.

The preferred and most direct way to assess the impact of annihilation topologies is to treat (x, σ) as free parameters in the fit and compare the resulting values of a_{sca} and ϕ_d with those obtained in the baseline Extended Fit. This defines the *floating-fit strategy*. In addition, we consider a strategy in which (x, σ) are scanned over the parameter space while being fixed point-by-point, retaining only the points that satisfy the acceptance criterion. This defines the *fixed-point strategy*, which is used as a cross-check of the floating-fit results and can also be used as an alternative when it is not feasible to leave all parameters free simultaneously. In this work, both strategies are applied and their results are compared. The overall structure of the E+A analysis is illustrated in the upper panel of Fig. 9.

Floating-fit strategy In the floating-fit strategy, the annihilation parameters (x, σ) are included directly in the fit as free parameters, as shown in the upper panel of Fig. 9. Hence, possible contributions from annihilation topologies are inherently accounted for in the fit. To remain consistent with the treatment of a_{sca}, we use the scan range $x \in [0, 1]$, where $x = 0$ denotes negligible contributions from annihilation topologies and $x = 1$ denotes contributions roughly comparable in size to the leading-order tree contribution (see Eq. (16)). The allowed size of these contributions is then constrained by the data within this range. To determine their impact, the resulting values of a_{sca} and ϕ_d are compared with those obtained in the baseline Extended Fit, corresponding to $x = 0$, where contributions from annihilation topologies are neglected. This strategy provides the most direct determination of the impact of annihilation topologies on the fit results.

Fixed-point strategy In the fixed-point strategy, illustrated schematically in the upper panel of Fig. 9, we scan over the considered parameter space of (x, σ) while keeping both parameters fixed point-by-point. The spread in the fitted values of a_{sca} and ϕ_d across the accepted scan points is then used to define an additional systematic uncertainty, which is added on top of the baseline result.

Procedure: fixed-point strategy

1. Define the scan range for (x, σ) and choose a fixed step size for both parameters.
2. Scan over the full parameter space of (x, σ), fixing both parameters point-by-point on this grid.
3. For each fixed point (x, σ), determine the best-fit central values of the parameters of interest, $a_{\rm sca}$ and ϕ_d, and compute the corresponding χ^2 value using `GammaCombo`.
4. Determine the global minimum $\chi^2_{\rm min}$ and compute
$$\Delta\chi^2 \equiv \chi^2 - \chi^2_{\rm min}$$
for each scanned point.
5. Accept only points satisfying $\Delta\chi^2 \leq 1$, corresponding to the 68% confidence-level interval for one parameter.
6. Using the accepted points, determine the minimum and maximum best-fit central values,
$$a_{\rm sca,min},\ a_{\rm sca,max}, \qquad \phi_{d,\rm min},\ \phi_{d,\rm max}.$$
7. The systematic uncertainty associated with annihilation contributions is then defined as
$$\delta^+_{\rm syst}(a_{\rm sca}) = a_{\rm sca,max} - a_{\rm sca,0}, \qquad \delta^-_{\rm syst}(a_{\rm sca}) = a_{\rm sca,0} - a_{\rm sca,min},$$
$$\delta^+_{\rm syst}(\phi_d) = \phi_{d,\rm max} - \phi_{d,0}, \qquad \delta^-_{\rm syst}(\phi_d) = \phi_{d,0} - \phi_{d,\rm min},$$
where $(a_{\rm sca,0}, \phi_{d,0})$ denote the baseline central values obtained for $x = 0$.
8. These systematic uncertainties are added on top of the baseline result.

6.2 E+A+R Fit

In Section 6.1, the E+A Fit was introduced, in which the annihilation parameters x and σ enter through the reparametrized CP asymmetries of the B^+ modes. To improve the constraints on these parameters, we now also include the ratio of CP-averaged branching fractions $\overline{\mathcal{R}}$. This defines the *Extended + Annihilation + Ratio* (E+A+R) Fit, illustrated in the lower panel of Fig. 9. As discussed in Section 5.2, the inclusion of $\overline{\mathcal{R}}$ introduces an additional parameter $\xi^{\mathcal{R}}$.

Accordingly, we first treat $\xi^{\mathcal{R}}$ as a free fit parameter. In this setup, the information from $\overline{\mathcal{R}}$ is mainly used to constrain $\xi^{\mathcal{R}}$ itself, allowing a lower and upper limit on $\xi^{\mathcal{R}}$ to be determined from the experimental data. We then impose $\xi^{\mathcal{R}}$ as an external Gaussian constraint, centered at different values between these limits. In this way, the information from $\overline{\mathcal{R}}$ acts as an additional constraint on x and σ. We then study how the fitted annihilation parameters depend on the assumed value of $\xi^{\mathcal{R}}$. The overall structure of this fit strategy is illustrated schematically in the lower panel of Fig. 9.

6.3 Future Projections

The analysis of the previous sections is repeated to study how the results change when the precision of the CP-asymmetry measurements and branching fraction ratios improves. In particular, the LHCb experiment is expected to collect an integrated luminosity $\mathcal{L}$ of 300 fb^{-1} by the end of the High-Luminosity LHC (HL-LHC) program [30], while Belle II is expected to accumulate 50 ab^{-1} [31]. Following the methodology of Ref. [5], the future uncertainties are projected by assuming that the statistical uncertainties scale as $1/\sqrt{\mathcal{L}}$, which follows from counting statistics. The systematic uncertainties and the correlations are kept unchanged as a conservative baseline assumption.

To construct these projections, we use the best-fit values of the fit parameters obtained from the current-data fits to recalculate the central values of the experimental inputs. In this way, we avoid artificial tensions between the input constraints when the statistical uncertainties are scaled down.

6.4 Experimental Inputs

For all experimental inputs not discussed explicitly here, we adopt the same values as in Ref. [5]. In this section, we summarize only the inputs relevant for the B^+ modes considered in the present analysis, and additionally include the ratio of CP-averaged branching fractions $\overline{\mathcal{R}}$ as a new input.

Direct CP asymmetry of $B^+ \to J/\psi\pi^+$ We use the following result from the LHCb collaboration [32]:

$$\mathcal{A}_{\rm CP}^{\rm dir}(B^+ \to J/\psi\pi^+) = (1.51 \pm 0.50 \pm 0.08) \cdot 10^{-2}. \tag{98}$$

This result is based on a combined data sample corresponding to an integrated luminosity of 8.4 fb^{-1}.

Direct CP asymmetry of $B^+ \to J/\psi K^+$ For the direct CP asymmetry of $B^+ \to J/\psi K^+$, we use the PDG average, which includes measurements from the CLEO2, BaBar, Belle, D0, and LHCb collaborations [13]:

$$\mathcal{A}_{\rm CP}^{\rm dir}(B^+ \to J/\psi K^+) = (1.8 \pm 3.0) \cdot 10^{-3}. \tag{99}$$

Branching fraction ratio $\overline{\mathcal{R}}$ As an additional input, we include the ratio of CP-averaged branching fractions defined in Eq. (74). For this ratio, we use the latest combined LHCb result [32]:

$$\overline{\mathcal{R}} = (3.846 \pm 0.018 \pm 0.018) \cdot 10^{-2}. \tag{100}$$

This result is based on a combined data sample corresponding to an integrated luminosity of 8.4 fb^{-1}.

7 Fit Results

This section presents the fit results following the methodology introduced in Section 6. The Nominal and Extended Fits provide the baseline for the analysis, which is subsequently generalized by including annihilation contributions in the E+A Fit, and finally by incorporating the branching fraction ratio $\overline{\mathcal{R}}$ in the E+A+R Fit.

7.1 Nominal and Extended Fits

We first reproduce the results for the Nominal and Extended Fits from Ref. [5], introduced in Section 3.1. In the Extended Fit, the direct CP asymmetries of the charged control modes $B^+ \to J/\psi\pi^+$ and $B^+ \to J/\psi K^+$ are included in addition to the Nominal Fit observables, while annihilation topologies in these charged modes are neglected.

Parameter	Nominal Fit	Extended Fit
a_{sca}	$0.136^{+0.135}_{-0.092}$	$0.130^{+0.134}_{-0.093}$
$\theta_{\text{sca}}\,[^\circ]$	167^{+21}_{-32}	$176.0^{+2.0}_{-9.3}$
$\phi_d\,[^\circ]$	$45.68^{+1.08}_{-0.99}$	$45.71^{+1.07}_{-0.99}$

Table 1: Best-fit values with asymmetric uncertainties obtained from one-dimensional likelihood scans in `GammaCombo` *for the Nominal and Extended Fits.*

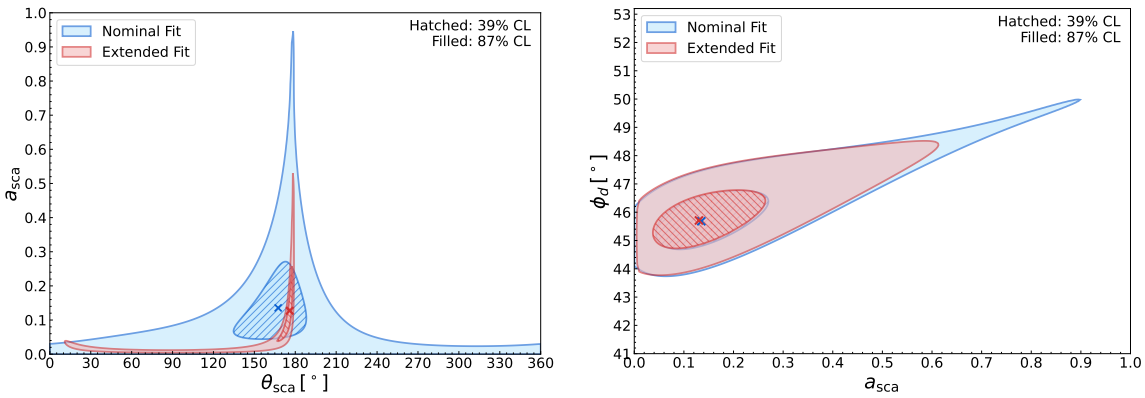

Figure 10: 39% (hatched) and 87% (filled) CL contours for the Nominal and Extended Fits, obtained with `GammaCombo`*. The best-fit points are indicated by crosses.*

As discussed in Ref. [5], Fig. 10 illustrates the impact of including the charged control modes. Following the interpretation given there, the main improvement is seen in the constraint on θ_{sca} rather than on a_{sca} itself. Consequently, the 39% confidence-level (CL) region in the (ϕ_d, a_{sca}) plane shown in Fig. 10 is not further reduced. However, as is also evident from Table 1, the inclusion of the B^+ modes leads to a small shift in the central value of a_{sca}, and consequently also in the central value of ϕ_d. Fig. 10 furthermore shows a clear positive correlation between ϕ_d and a_{sca}, as reported in Ref. [5], which demonstrates the sensitivity of the determined value of ϕ_d to a_{sca}. In contrast, Fig. 11 shows no significant correlation between θ_{sca} and ϕ_d.

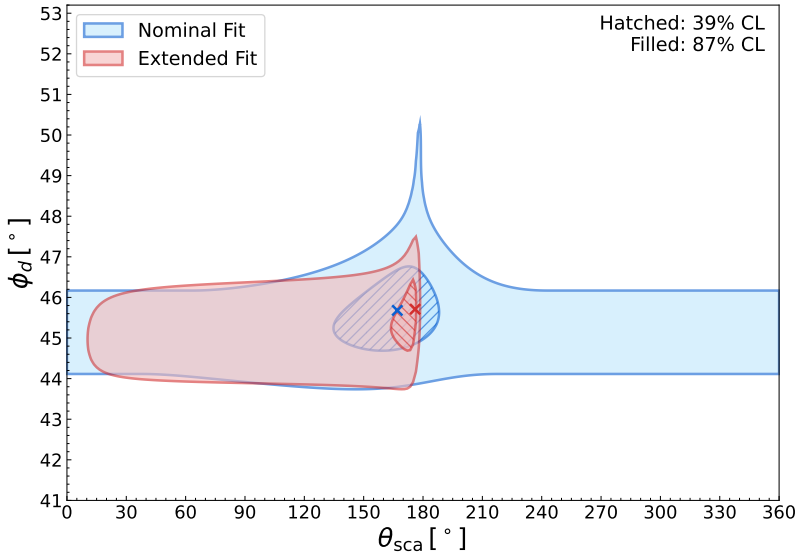

Figure 11: 39% (hatched) and 87% (filled) CL regions for the Nominal and Extended Fits, obtained with `GammaCombo`*. The best-fit points are indicated by crosses.*

We now investigate how the picture changes when contributions from annihilation topologies are explicitly included.

7.2 E+A Fit

7.2.1 Floating-fit Results

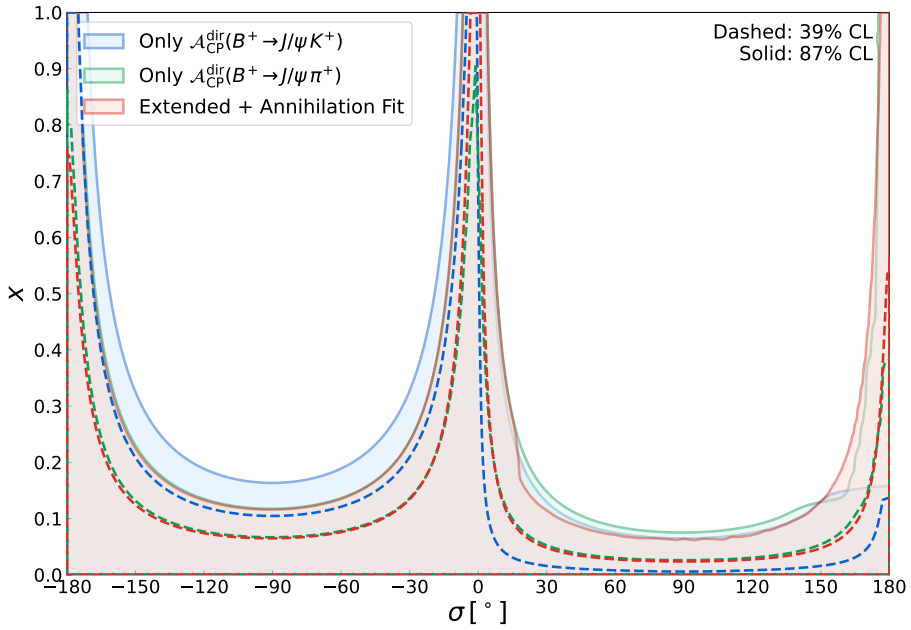

Figure 12: 39% CL (dashed) and 87% CL (solid) contours obtained from the `GammaCombo` *fit, shown separately for the constraints from the $B^+ \to J/\psi\pi^+$ mode, the $B^+ \to J/\psi K^+$ mode, and their combined treatment in the Extended + Annihilation Fit.*

Constraint on (x, σ) The two-dimensional confidence-level contours for the annihilation parameters (x, σ) are shown in Fig. 12.

The 39% CL contours, corresponding to $\Delta\chi^2 \leq 1$, cover the full scan ranges, $x \in [0, 1]$ and $\sigma \in [-180°, 180°]$, and no unique best-fit solution (x, σ) is found. This indicates that the system remains underconstrained by the current data. At the same time, $x = 0$ lies inside the allowed region and is therefore fully compatible with the fit.

The origin of the underconstrained nature of the fit can be understood by comparing the individual decay-mode constraints in Fig. 12. The contours from the $B^+ \to J/\psi\pi^+$ and $B^+ \to J/\psi K^+$ CP asymmetries exhibit similar dependencies in the (x, σ) plane and are therefore not sufficiently complementary. In addition, the sensitivity of the $B^+ \to J/\psi K^+$ mode to x is suppressed by a factor of ϵ (see Eq. (25)), so that its contribution to the total χ^2 remains comparatively small over most of the relevant parameter space. As a result, the combined fit is effectively dominated by the $B^+ \to J/\psi\pi^+$ mode, and the Extended + Annihilation contours overlap with those obtained from the $B^+ \to J/\psi\pi^+$ mode alone, as is evident from Fig. 12.

Consequently, combining both modes does not significantly improve the determination of (x, σ). With the current inputs, the annihilation parameters therefore remain only weakly constrained.

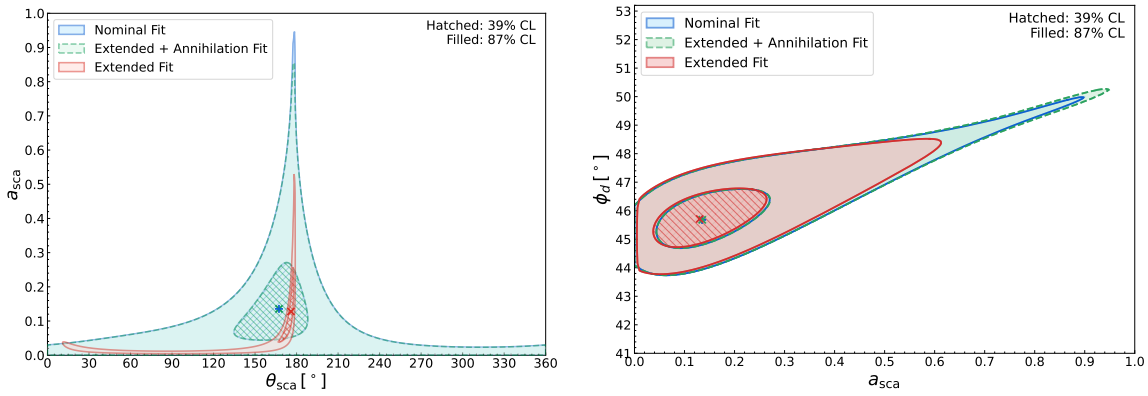

Figure 13: 39% *(hatched) and* 87% *(filled) CL regions obtained with* `GammaCombo` *for the Nominal, Extended, and E+A Fits, with the best-fit points indicated by crosses.*

Comparison with the Nominal and Extended Fits We now compare the E+A Fit with the Nominal Fit and the Extended Fit. As can be seen from Table 2 and Fig. 13, the E+A Fit reproduces the same values for the pseudoscalar-sector fit parameters as the Nominal Fit. This can be understood as follows: once the annihilation parameters (x, σ) are introduced as additional free parameters, the CP asymmetries of $B^+ \to J/\psi\pi^+$ and $B^+ \to J/\psi K^+$ are primarily used to constrain (x, σ), rather than providing additional constraints on the penguin parameters $(a_{\rm sca}, \theta_{\rm sca})$.

The vector-sector parameters in the E+A Fit instead agree with those of the Extended Fit. This difference with respect to the Nominal Fit is due to the inclusion of the additional mode $B_s^0 \to J/\psi \bar{K}^{*0}$ in the Extended and E+A Fits. The small difference between the Extended Fit and the other two fits in the $B \to D\bar{D}$ sector is due to the corresponding small shift in the best-fit value of ϕ_d.

Parameter	Nominal Fit	Extended Fit	E+A Fit
$a_{\rm sca}$	$0.136^{+0.135}_{-0.092}$	$0.130^{+0.134}_{-0.093}$	$0.136^{+0.135}_{-0.092}$
$\theta_{\rm sca}$ [°]	167^{+21}_{-32}	$176.0^{+2.1}_{-9.3}$	167^{+21}_{-32}
ϕ_d [°]	$45.68^{+1.08}_{-0.99}$	$45.71^{+1.07}_{-0.99}$	$45.68^{+1.08}_{-0.99}$
$a_{\rm vec}$	$0.053^{+0.091}_{-0.046}$	$0.044^{+0.097}_{-0.044}$	$0.044^{+0.097}_{-0.044}$
$\theta_{\rm vec}$ [°]	318^{+37}_{-121}	334^{+26}_{-334}	334^{+26}_{-334}
ϕ_s [rad]	$-0.065^{+0.018}_{-0.017}$	$-0.065^{+0.018}_{-0.017}$	$-0.065^{+0.018}_{-0.017}$
$a_{\rm DD}$	$0.0082^{+0.0536}_{-0.0082}$	$0.0085^{+0.0535}_{-0.0085}$	$0.0082^{+0.0536}_{-0.0082}$
$\theta_{\rm DD}$ [°]	$351.1^{+8.9}_{-351.1}$	$351.4^{+8.6}_{-351.4}$	$351.1^{+8.9}_{-351.1}$
x	–	–	$0.56^{+0.44}_{-0.56}$ $(*)$
σ [°]	–	–	-2^{+182}_{-178} $(*)$

Table 2: Best-fit values with asymmetric uncertainties obtained from one-dimensional likelihood scans in `GammaCombo` *for the Nominal, Extended, and Extended + Annihilation (E+A) Fits.*
$(*)$ *One of the degenerate minima. The corresponding interval also reaches the scan boundaries.*

To evaluate the impact of the contributions from annihilation topologies, we take the Extended Fit as the baseline and compare its fitted central values with those obtained in the E+A Fit. The corresponding central values and uncertainties, determined from the one-dimensional likelihood scans, are listed in Table 2. For the quoted 68% intervals, we define the interval width as

$$\Delta^{68} \equiv \sigma^{+} + \sigma^{-}, \tag{101}$$

where σ^{+} and σ^{-} denote the upper and lower uncertainties, respectively.

The shift due to the inclusion of annihilation topologies is defined as the absolute difference between the best-fit central values obtained in the E+A Fit and those of the Extended Fit. Since no correlation is observed between $\theta_{\rm sca}$ and ϕ_d (see Fig. 11), the comparison is restricted to $a_{\rm sca}$ and ϕ_d. This gives

$$|\delta a_{\rm sca}| = 0.006, \quad |\delta \phi_d| = 0.03^{\circ}. \tag{102}$$

Using the experimental 68% interval widths from the Extended Fit,

$$\Delta^{68}_{\rm exp}(a_{\rm sca}) = 0.227, \qquad \Delta^{68}_{\rm exp}(\phi_d) = 2.06^{\circ}, \tag{103}$$

we obtain

$$\frac{|\delta a_{\rm sca}|}{\Delta^{68}_{\rm exp}(a_{\rm sca})} \simeq 0.03, \qquad \frac{|\delta \phi_d|}{\Delta^{68}_{\rm exp}(\phi_d)} \simeq 0.01. \tag{104}$$

Hence, the shifts induced by contributions from annihilation topologies correspond to only about 3% and 1% of the experimental 68% interval widths for $a_{\rm sca}$ and ϕ_d, respectively.

Correlations Besides the (x, σ) contour, Fig. 14 shows the corresponding $(x, a_{\rm sca})$ and (x, ϕ_d) contours. No significant correlation is observed between x and either $a_{\rm sca}$ or ϕ_d.

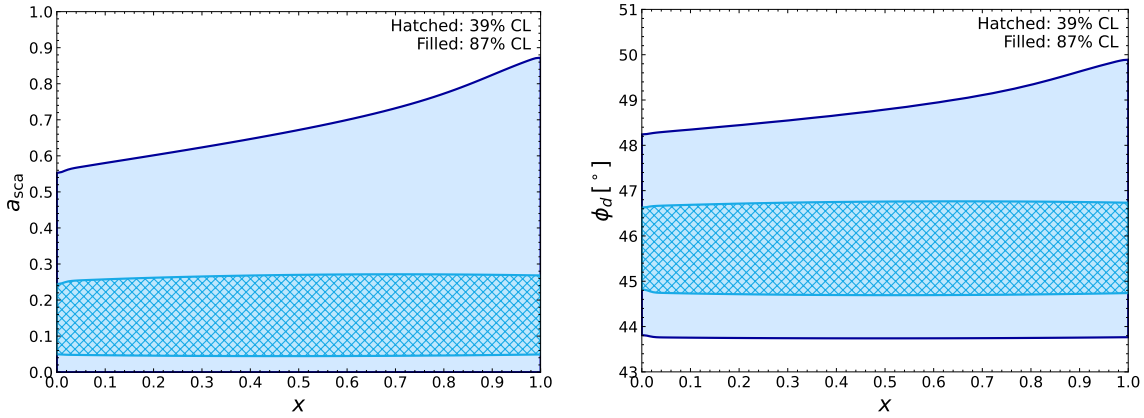

Figure 14: 39% *(hatched) and* 87% *(filled) CL regions obtained with* `GammaCombo` *for the E+A Fit.*

7.2.2 Fixed-point Results

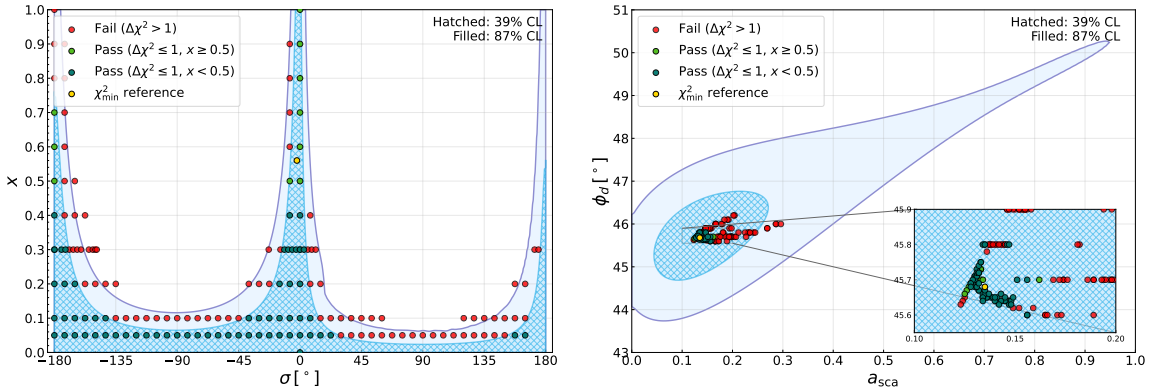

Figure 15: Comparison of the fixed-point and floating-fit results including annihilation contributions. The 39% CL (hatched) and 87% CL (filled) regions obtained with `GammaCombo` *are overlaid with the sampled points from the fixed-point scan.*

Figure 15 compares the results obtained from the fixed-point and floating-fit strategies. The floating fit yields the `GammaCombo` confidence-level contours, while the fixed-point strategy gives the accepted and rejected scan points shown in the figure.

The reference value of $\chi^2_{\rm min}$ is taken from the degenerate minimum listed in Table 2,

$$x = 0.56, \qquad \sigma = -2^\circ. \tag{105}$$

Importantly, in the (x, σ) plane, all points accepted by the fixed-point scan lie within the 39% confidence-level contour of the floating fit. This confirms that the acceptance criterion $\Delta\chi^2 \leq 1$ indeed corresponds to the usual 68% interval, since, as discussed in Section 3.1, the 39% CL contour in two dimensions corresponds to the 68% interval in one-dimensional scans.

In the $(\phi_d, a_{\rm sca})$ plane, some rejected points nevertheless appear inside the 39% contour. This is not contradictory, since the acceptance criterion is applied in the scanned (x, σ) plane. Hence, a point may lie outside the 39% CL region in the (x, σ) plane while still falling inside the 39% CL region in the projected $(\phi_d, a_{\rm sca})$ plane.

The points with $x < 0.5$ have also been marked explicitly. As can be seen from Fig. 15, these points are not systematically farther away from the $\chi^2_{\rm min}$ reference point than the points with $x \geq 0.5$. This is consistent with the conclusion from Fig. 14 that there is no strong correlation between x and either $a_{\rm sca}$ or ϕ_d. Consequently, the outer points in the $(\phi_d, a_{\rm sca})$ plane are not expected to originate systematically from either small or large values of x. Restricting the scan range by imposing a smaller upper bound on x by hand would therefore not lead to a significant change in the extremal values of $a_{\rm sca}$ and ϕ_d. For this reason, and to keep the procedure consistent, we continue to use the full scan range $x \in [0, 1]$.

From the accepted scan points, we obtain

$$a_{\rm sca,min} = 0.125, \qquad a_{\rm sca,max} = 0.162, \tag{106}$$

$$\phi_{d,\rm min} = 45.6^\circ, \qquad \phi_{d,\rm max} = 45.8^\circ. \tag{107}$$

Using the Extended Fit as the baseline, these ranges are interpreted as the systematic uncertainty associated with contributions from annihilation topologies, which we add on top of this baseline result. Quoting this separately from the experimental uncertainty, we obtain

$$a_{\rm sca} = 0.130^{+0.134}_{-0.093}\,({\rm exp})\,^{+0.032}_{-0.005}\,({\rm syst}), \tag{108}$$

$$\phi_d = \left(45.71^{+1.07}_{-0.99}\,({\rm exp})\,^{+0.09}_{-0.11}\,({\rm syst})\right)^\circ. \tag{109}$$

Using the definition of the 68% interval width in Eq. (101), this gives

$$\Delta^{68}_{\rm exp}(a_{\rm sca}) = 0.227, \qquad \Delta^{68}_{\rm syst}(a_{\rm sca}) = 0.037, \tag{110}$$

$$\Delta^{68}_{\rm exp}(\phi_d) = 2.06^\circ, \qquad \Delta^{68}_{\rm syst}(\phi_d) = 0.20^\circ. \tag{111}$$

Hence,

$$\frac{\Delta^{68}_{\rm syst}(a_{\rm sca})}{\Delta^{68}_{\rm exp}(a_{\rm sca})} \simeq 0.16, \qquad \frac{\Delta^{68}_{\rm syst}(\phi_d)}{\Delta^{68}_{\rm exp}(\phi_d)} \simeq 0.10. \tag{112}$$

For both $a_{\rm sca}$ and ϕ_d, the systematic uncertainties due to contributions from annihilation topologies are significantly smaller than the corresponding experimental uncertainties. Compared with the results from the floating-fit strategy, Eq. (102), the systematic uncertainties obtained from the fixed-point scan are larger. This can be explained by the different ways in which the effect of annihilation contributions is quantified in the two strategies. In the floating-fit strategy, x and σ are treated as free fit parameters. By contrast, in the fixed-point strategy, (x, σ) are forced to specific values over the allowed parameter space. The remaining fit parameters, in particular $a_{\rm sca}$ and ϕ_d, therefore readjust for each fixed point (x, σ), leading to a larger spread in their best-fit central values. The fixed-point strategy therefore yields a more conservative estimate.

Even with this more conservative approach, the systematic uncertainty on ϕ_d amounts to only about 10% of the corresponding experimental uncertainty. Thus, we conclude that the impact of contributions from annihilation topologies is negligible given the current experimental precision.

7.3 E+A+R Fit

7.3.1 $\xi^{\mathcal{R}}$ as a Free Parameter

For the E+A+R Fit, we begin with the most general setup, in which $\xi^{\mathcal{R}}$ is treated as a free parameter and determined directly from the experimental data. Since including the ratio of CP-averaged branching fractions $\overline{\mathcal{R}}$ introduces one additional observable but also one additional free parameter in this case, the inclusion of $\overline{\mathcal{R}}$ primarily constrains $\xi^{\mathcal{R}}$ itself rather than providing an additional constraint on (x, σ). Consequently, the resulting (x, σ) contour is identical to that obtained in the E+A Fit, shown in Fig. 12.

The confidence-level regions in the $(x, \xi^{\mathcal{R}})$ plane are shown in Fig. 16.

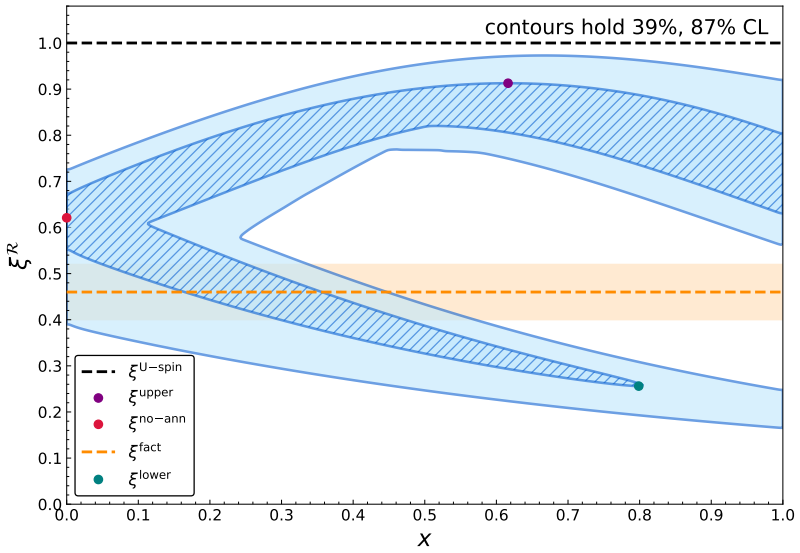

Figure 16: 39% (hatched) and 87% (filled) CL regions obtained with `GammaCombo` *for the E+A+R Fit with $\xi^{\mathcal{R}}$ treated as a free parameter.*

Figure 16 shows a strong correlation between x and $\xi^{\mathcal{R}}$. As in the E+A Fit, no unique minimum in x is obtained, and consequently no unique minimum in $\xi^{\mathcal{R}}$ can be identified either. A precise determination of $\xi^{\mathcal{R}}$ in this way is therefore not feasible, since the annihilation parameters remain underconstrained.

Nevertheless, we can still determine the allowed range of $\xi^{\mathcal{R}}$ at 68% CL by finding its extreme values within the corresponding two-dimensional 39% CL region in Fig. 16. These are given by

$$(x, \xi^{\text{upper}}) = (0.62,\ 0.91), \tag{113}$$

$$(x, \xi^{\text{lower}}) = (0.80,\ 0.26). \tag{114}$$

Comparing the different benchmark cases, the factorizable estimate from Eq. (88) lies within the 39% CL region, whereas the value $\xi^{\text{U-spin}} = 1$ is excluded by the experimental data at 95% CL. This is consistent with the expectation that $\xi^{\mathcal{R}}$ receives significant factorizable and non-factorizable symmetry-breaking contributions.

If we assume that contributions from annihilation topologies are negligible, i.e. set $x = 0$, we obtain

$$\xi^{\text{no-ann}} = 0.621^{+0.059}_{-0.084}. \tag{115}$$

Using Eq. (92), this corresponds to an effective non-factorizable symmetry-breaking factor

$$\kappa^{\text{no-ann}} = 1.35^{+0.22}_{-0.25}, \tag{116}$$

which implies non-factorizable symmetry breaking with a central value of 35%, although the uncertainties are still relatively large. A sizable non-factorizable effect is not unexpected, since the decay proceeds at leading order through a color-suppressed tree topology, for which such contributions are expected to be significant.

The corresponding constraints in the (x, κ) plane are shown in Fig. 17.

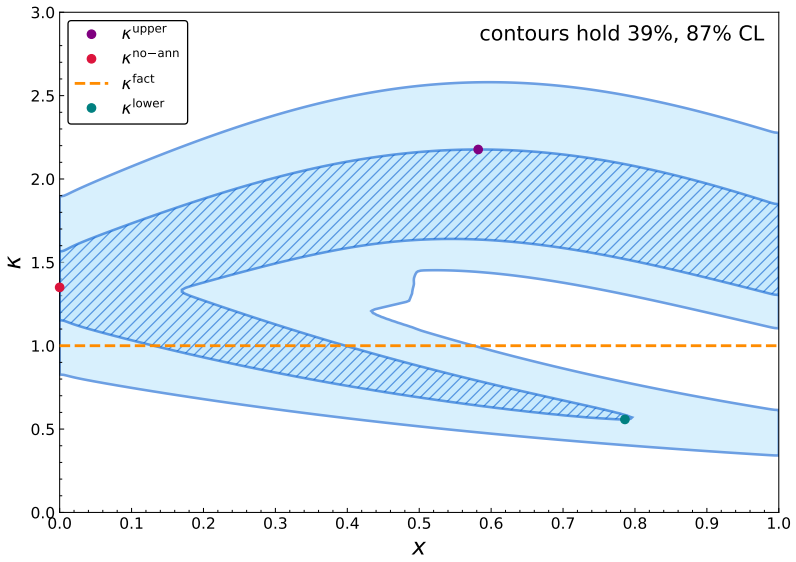

Figure 17: 39% (hatched) and 87% (filled) CL regions obtained with `GammaCombo` *for the E+A+R Fit with κ treated as a free parameter.*

Analogously to the $\xi^{\mathcal{R}}$ case, we determine the extreme values of κ within the 39% CL region:

$$(x, \kappa^{\text{upper}}) = (0.58,\, 2.18), \tag{117}$$

$$(x, \kappa^{\text{lower}}) = (0.79,\, 0.56). \tag{118}$$

The relevant benchmark values of $\xi^{\mathcal{R}}$ and κ discussed in this subsection are summarized in Table 3.

Case	$\xi^{\mathcal{R}}$	κ
39% CL lower point	0.26	0.56
Factorizable limit	0.47 ± 0.07	1
No annihilation ($x = 0$)	$0.621^{+0.059}_{-0.084}$	$1.35^{+0.22}_{-0.25}$
39% CL upper point	0.91	2.18
U-spin symmetry	1	–

Table 3: Summary of benchmark values for $\xi^{\mathcal{R}}$ and κ. The entries labeled as upper and lower correspond to the extreme values within the 39% CL regions.

7.3.2 $\xi^{\mathcal{R}}$ as a Gaussian Constraint

Table 3 shows that the allowed range of $\xi^{\mathcal{R}}$ is still quite broad. Since our aim is to use $\overline{\mathcal{R}}$ to further constrain the annihilation parameters (x, σ), we adopt an agnostic approach in which $\xi^{\mathcal{R}}$ is treated as an external input, rather than a free parameter. Due to this broad allowed range, we consider four Gaussian constraints within the 68% CL interval of $\xi^{\mathcal{R}}$:

$$\xi^{\mathcal{R}} = 0.50 \pm 0.05, \quad \xi^{\mathcal{R}} = 0.60 \pm 0.05, \quad \xi^{\mathcal{R}} = 0.70 \pm 0.05, \quad \xi^{\mathcal{R}} = 0.80 \pm 0.05. \tag{119}$$

The resulting contours in the (x, σ) plane are shown in Fig. 18, while the corresponding best-fit values are summarized in Table 4.

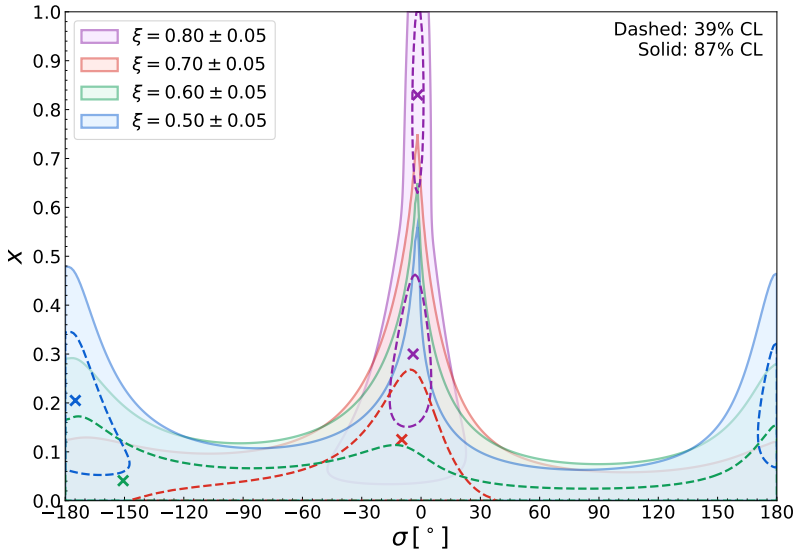

Figure 18: 39% CL (dashed) and 87% CL (solid) contours for the annihilation parameters (x, σ), obtained with `GammaCombo` in the E+A+R Fit with $\xi^{\mathcal{R}}$ imposed as a Gaussian constraint. The best-fit points are indicated by crosses.

$\xi^{\mathcal{R}}$	x	$\sigma\,[^\circ]$	$a_{\rm sca}$	$\theta_{\rm sca}\,[^\circ]$	$\phi_d\,[^\circ]$
0.50 ± 0.05	$0.21^{+0.14}_{-0.16}$	-175^{+27}_{-5}	$0.136^{+0.135}_{-0.092}$	167^{+11}_{-32}	$45.68^{+1.08}_{-0.99}$
0.60 ± 0.05	$0.048^{+0.125}_{-0.048}$	$-155^{+335\ (*)}_{-25}$	$0.135^{+0.136}_{-0.091}$	167^{+11}_{-32}	$45.68^{+1.08}_{-0.99}$
0.70 ± 0.05	$0.12^{+0.15}_{-0.12}$	$-11^{+191\ (*)}_{-169}$	$0.136^{+0.135}_{-0.092}$	167^{+21}_{-32}	$45.68^{+1.08}_{-0.99}$
0.80 ± 0.05	$0.29^{+0.18}_{-0.14}$	$-4.6^{+9.7}_{-11.5}$	$0.136^{+0.135}_{-0.092}$	167^{+21}_{-32}	$45.68^{+1.08}_{-0.99}$
	$0.84^{+0.16\ (**)}_{-0.23}$	$-1.7^{+6.9}_{-14.3}$	$0.136^{+0.135}_{-0.092}$	167^{+21}_{-32}	$45.68^{+1.08}_{-0.99}$

Table 4: Central values and asymmetric uncertainties obtained for different Gaussian inputs of $\xi^{\mathcal{R}}$.
$(*)$ *Fully consistent with the scan range within one standard deviation.*
$(**)$ *The upper limit coincides with the upper boundary of the scan range.*

From Fig. 18 and Table 4, we observe that including information from $\overline{\mathcal{R}}$ significantly improves the constraints on the annihilation parameters relative to the E+A Fit (cf. Fig. 12 and Table 2). In contrast to the E+A Fit with x and σ treated as free parameters, the E+A+R Fit yields well-defined best-fit solutions for x and σ once $\xi^{\mathcal{R}}$ is provided as an external input. By comparison, Table 4 also shows that the fitted pseudoscalar-sector parameters do not differ from those obtained in the Nominal Fit shown in Table 2, nor do they exhibit any dependence on $\xi^{\mathcal{R}}$. This is expected, since in the E+A Fit the B^+ modes primarily constrain (x, σ) rather than the pseudoscalar-sector parameters. Hence, in the E+A+R Fit, the inclusion of $\overline{\mathcal{R}}$ acts as an additional constraint on (x, σ), rather than on the pseudoscalar-sector parameters, leaving them unchanged.

At the same time, Table 4 shows that for most choices of $\xi^{\mathcal{R}}$, the best-fit value of x is of the same order as $a_{\rm sca}$, although the associated uncertainties remain large. Consequently, these results are not yet sufficient to definitively establish the expected hierarchy $x \ll a_{\rm sca}$. The primary reason is the limited orthogonality of the constraints from the CP asymmetries and $\overline{\mathcal{R}}$ in parameter space. A secondary reason is the limited experimental precision of the CP asymmetries.

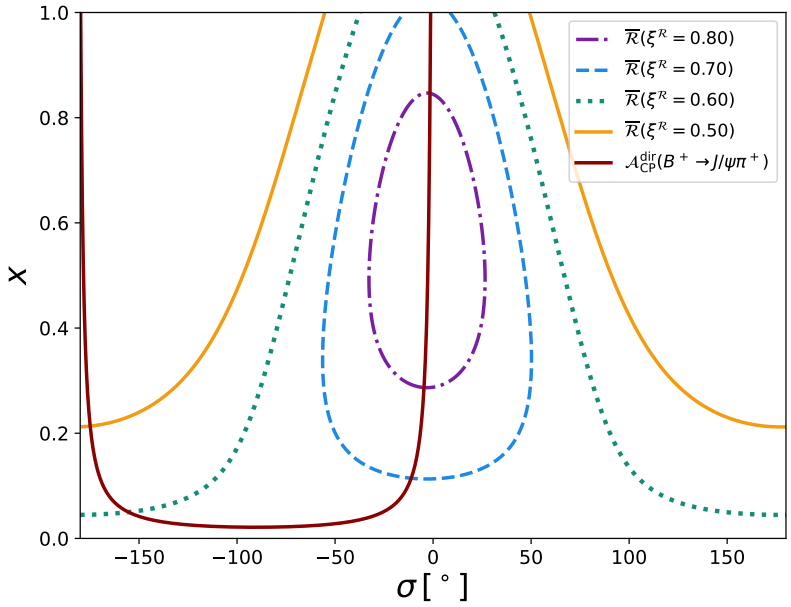

Figure 19: Overlap of the contour constraints from $\mathcal{A}_{CP}^{dir}(B^+ \to J/\psi\pi^+)$ and $\overline{\mathcal{R}}$ for different fixed values of $\xi^{\mathcal{R}}$. The contours are obtained for fixed fit parameters $a_{sca} = 0.136$, $\theta_{sca} = 167°$, $\gamma = 65.6°$, and $\lambda = 0.22308$, and fixed central values of the observables.

To illustrate this primary limitation, Fig. 19 shows the separate constraints from $\mathcal{A}_{\mathrm{CP}}^{\mathrm{dir}}(B^+ \to J/\psi\pi^+)$ and $\overline{\mathcal{R}}$ in the (x, σ) plane. Around $\sigma \simeq 0°$, both contours are elongated in the x-direction, showing that the constraints are not sufficiently orthogonal. As a result, x remains weakly constrained particularly in this region, as is also evident from the CL regions in Fig. 18. The secondary limitation will be discussed in more detail in Section 7.4.

Finally, we note that the best-fit solutions depend strongly on the assumed value of $\xi^{\mathcal{R}}$, as is evident from Fig. 18. This is consistent with Fig. 16, which shows a strong dependence of x on $\xi^{\mathcal{R}}$. In particular, for $\xi^{\mathcal{R}} = 0.60 \pm 0.05$, the behavior differs significantly from the other cases: the fitted value of σ remains fully compatible with the scan range $\sigma \in [-180°, 180°]$ within one standard deviation, consistent with the fact that x is compatible with zero at the same confidence level. Due to this strong dependence of the fitted annihilation parameters on $\xi^{\mathcal{R}}$, a more precise determination of $\xi^{\mathcal{R}}$ is essential if $\overline{\mathcal{R}}$ is to be used as an additional input.

7.4 Future Projections

To assess how the results may improve with increased experimental precision, we now turn to future projections for the Extended Fit, the E+A Fit, and the E+A+R Fit. As discussed in Section 6.3, the central values of the experimental inputs are recalculated using the best-fit values of the fit parameters obtained from the current-data fits. The statistical uncertainties are then projected by luminosity scaling, while the systematic uncertainties and correlations are kept unchanged.

For $\mathcal{A}_{\mathrm{CP}}^{\mathrm{dir}}(B^+ \to J/\psi\pi^+)$, we use the LHCb measurement given in Eq. (98) as the current-data baseline. For $\mathcal{A}_{\mathrm{CP}}^{\mathrm{dir}}(B^+ \to J/\psi K^+)$, we use the LHCb measurement underlying the most recent PDG average used in our analysis [33],

$$\mathcal{A}_{\mathrm{CP}}^{\mathrm{dir}}(B^+ \to J/\psi K^+) = (0.9 \pm 2.7 \pm 0.7) \times 10^{-3}. \tag{120}$$

This measurement is based on the full Run 1 LHCb dataset, corresponding to an integrated luminosity of 3 fb^{-1}. For the ratio of CP-averaged branching fractions $\overline{\mathcal{R}}$, we use the LHCb measurement given in Eq. (100). Since all these current-data baselines are based on LHCb measurements, their statistical uncertainties are projected using the expected end-of-HL-LHC luminosity discussed in Section 6.3.

7.4.1 Extended Fit

Using the best-fit values of the fit parameters given in Table 2, we recalculate the CP-asymmetry inputs for the projected future dataset. The resulting values are listed in Table E.1 in the Appendix. The corresponding fit results are summarized in Table 5, where they are compared with those obtained from the current dataset. A significant reduction in the uncertainties is observed for all three fitted quantities.

Parameter	Current Data	Future Data
a_{sca}	$0.130^{+0.134}_{-0.093}$	$0.131^{+0.033}_{-0.031}$
$\theta_{\mathrm{sca}}\,[^\circ]$	$176.0^{+2.1}_{-9.3}$	$176.0^{+0.5}_{-1.5}$
$\phi_d\,[^\circ]$	$45.71^{+1.07}_{-0.99}$	$45.72^{+0.21}_{-0.21}$

Table 5: Best-fit values and asymmetric uncertainties obtained from one-dimensional likelihood scans in `GammaCombo` *for the Extended Fit, comparing the current dataset with the projected future scenario based on the expected end-of-HL-LHC and Belle II precision.*

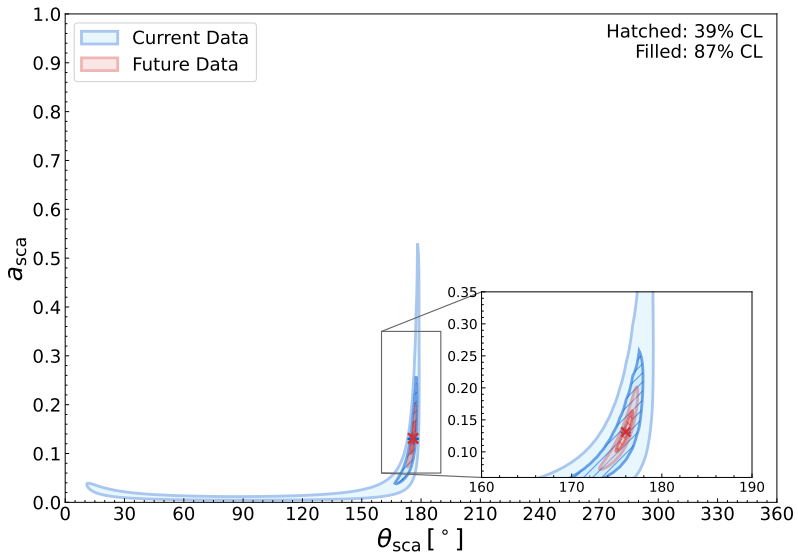

Figure 20: 39% *(hatched) and* 87% *(filled) CL regions obtained with* `GammaCombo` *for the Extended Fit, comparing the current dataset with the projected future scenario based on the expected end-of-HL-LHC and Belle II precision. The best-fit points are indicated by crosses.*

The further tightening of the constraints is also evident in Fig. 20, where the allowed region in the $(a_{\text{sca}}, \theta_{\text{sca}})$ plane becomes substantially smaller for the projected future dataset. In particular, in this scenario, a_{sca} can be tightly constrained.

7.4.2 E+A Fit

Floating-fit strategy We now apply the same procedure to the E+A Fit. Using the best-fit values of the fit parameters from Table 2, we recalculate the CP-asymmetry inputs for the projected future dataset. These updated inputs are given in Table E.1 in the Appendix. The corresponding results are shown in Table 6, together with the E+A Fit results for current data and the projected results of the Extended Fit.

Parameter	E+A Fit Current Data	E+A Fit Future Data	Extended Fit Future Data
a_{sca}	$0.136^{+0.135}_{-0.092}$	$0.135^{+0.034}_{-0.030}$	$0.131^{+0.033}_{-0.031}$
$\theta_{\text{sca}}\,[^\circ]$	167^{+21}_{-32}	$167.1^{+7.5}_{-8.3}$	$176.0^{+0.5}_{-1.5}$
$\phi_d\,[^\circ]$	$45.68^{+1.08}_{-0.99}$	$45.68^{+0.29}_{-0.27}$	$45.72^{+0.21}_{-0.21}$

Table 6: Comparison of the best-fit values and asymmetric uncertainties obtained from one-dimensional likelihood scans in `GammaCombo` *for the E+A Fit with current data, and for the E+A and Extended Fits in the projected future scenario based on the expected end-of-HL-LHC and Belle II precision.*

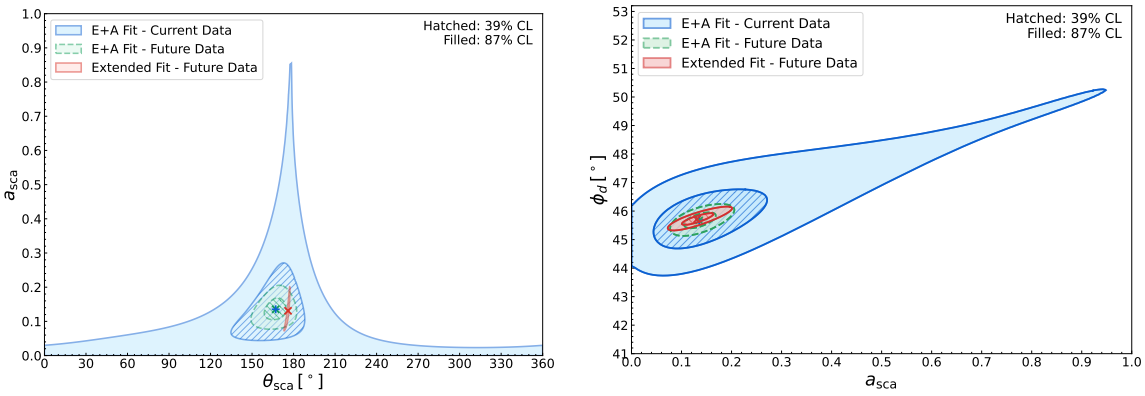

Figure 21: 39% (hatched) and 87% (filled) CL regions comparing the current-data E+A Fit with the E+A and Extended Fits in the projected future scenario based on the expected end-of-HL-LHC and Belle II precision. The best-fit points are indicated by crosses.

From Table 6 and Fig. 21, we observe that the future projections lead to a significant reduction in the uncertainties on both a_{sca} and θ_{sca}.

A comparison of the future E+A Fit with the future Extended Fit shows that there is no significant difference in the uncertainty on a_{sca}, whereas the main difference appears in the uncertainty on θ_{sca}. This is also clearly visible in the left panel of Fig. 21.

This behavior is expected. As discussed in Section 7.1, the inclusion of the B^+ observables primarily improves the determination of θ_{sca}, while having only a limited impact on the uncertainty of a_{sca}. In the future E+A Fit, however, these observables primarily constrain the annihilation parameters x and σ, which weakens the constraining power on θ_{sca} relative to the future Extended Fit.

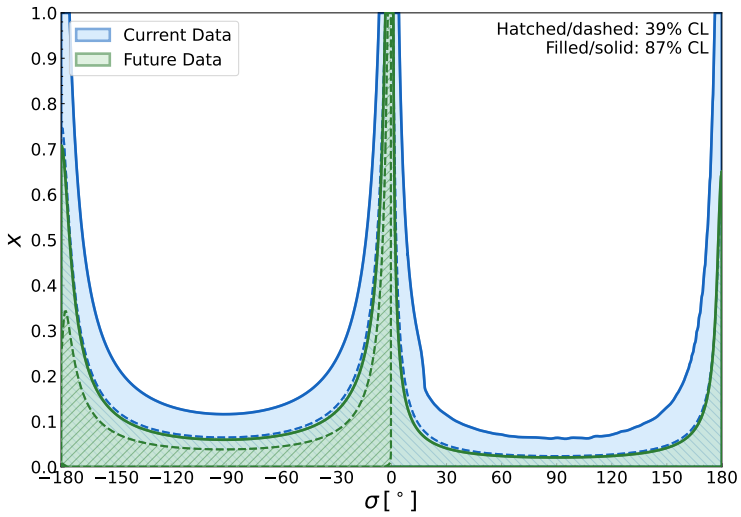

Figure 22: Confidence-level contours for the annihilation parameters (x, σ) in the E+A Fit, obtained with `GammaCombo` *for the current dataset and the projected future scenario based on the expected end-of-HL-LHC and Belle II precision.*

In Fig. 22, the confidence-level regions obtained from the current data are compared with those expected from the future projections. A significant reduction of the confidence-level regions is observed. However, future projections do not change the orthogonality of the constraints in parameter space. Hence, it is still not possible to determine unique best-fit values for x and σ, and both parameters remain underconstrained.

Fixed-point strategy Figure 23 compares the results obtained from the fixed-point and floating-fit strategies in the projected future scenario.

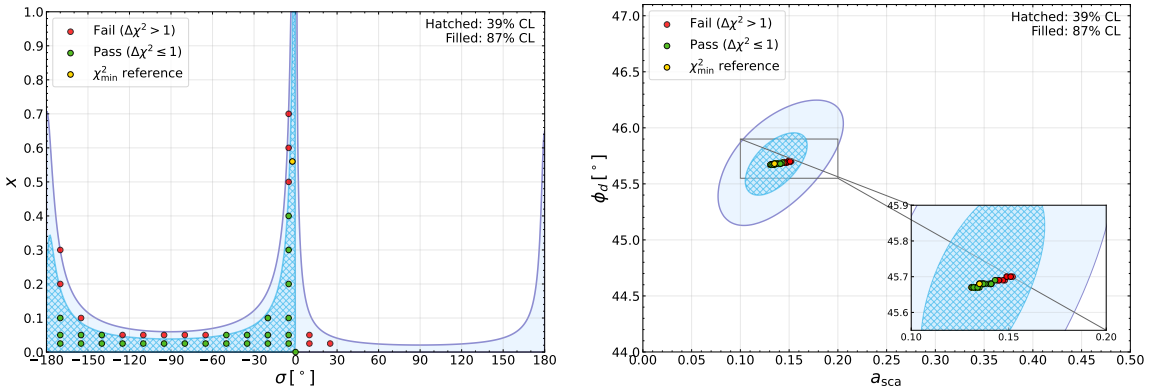

Figure 23: Comparison of the fixed-point and floating-fit results including annihilation contributions in the projected future scenario based on the expected end-of-HL-LHC and Belle II precision. The 39% CL (hatched) and 87% CL (filled) regions obtained with `GammaCombo` *are overlaid with the sampled points from the fixed-point scan.*

As in the current-data case, the fixed-point scan is evaluated with respect to the same reference minimum given by Eq. (105), indicated by the golden point in Fig. 23. In the left panel, all points accepted by the fixed-point procedure lie within the 39% confidence-level contour of the fit from the floating-fit strategy, again confirming the consistency between the fixed-point and floating-fit strategies.

Using the future Extended Fit result quoted in Table 6 as the baseline, and applying the same fixed-point procedure as in the current-data case, we obtain

$$a_{\text{sca}} = 0.131^{+0.033}_{-0.031}\,(\text{exp})\,^{+0.012}_{-0.000}\,(\text{syst}), \tag{121}$$

$$\phi_d = \left(45.72^{+0.21}_{-0.21}\,(\text{exp})\,^{+0.00}_{-0.05}\,(\text{syst})\right)^\circ. \tag{122}$$

With the 68% interval-width definition of Eq. (101), the corresponding current- and future-data results are summarized in Table 7.

	a_{sca}			ϕ_d		
Scenario	Δ^{68}_{exp}	$\Delta^{68}_{\text{syst}}$	$\Delta^{68}_{\text{syst}}/\Delta^{68}_{\text{exp}}$	Δ^{68}_{exp}	$\Delta^{68}_{\text{syst}}$	$\Delta^{68}_{\text{syst}}/\Delta^{68}_{\text{exp}}$
Current data	0.227	0.037	0.16	2.06°	0.20°	0.10
Future data	0.064	0.012	0.19	0.42°	0.05°	0.12

Table 7: Comparison of the experimental and systematic 68% interval widths obtained with the fixed-point strategy for the current dataset and the projected future scenario based on the expected end-of-HL-LHC and Belle II precision.

Table 7 shows clearly that both the experimental and systematic 68% interval widths become significantly smaller in the future scenario. At the same time, the relative size of the

systematic uncertainties associated with annihilation topologies remains similar, as can be seen from the ratios $\Delta^{68}_{\text{syst}}/\Delta^{68}_{\text{exp}}$ for current and future data. Thus, the conclusion remains unchanged in the projected future case: for both observables, the systematic uncertainty induced by annihilation topologies is significantly smaller than the experimental uncertainty. This is also visible directly in Fig. 23, where the accepted fixed-point scan points induce only a small spread in a_{sca} and ϕ_d compared with the projected experimental precision. Thus, we conclude that the impact of contributions from annihilation topologies remains negligible even at the projected experimental precision considered in this future scenario.

7.4.3 E+A+R Fit

$\xi^{\mathcal{R}}$ as a free parameter For the E+A+R Fit, we again start from the most general setup, in which $\xi^{\mathcal{R}}$ is treated as a free parameter, and investigate how strongly it could be constrained once the projected end-of-HL-LHC and Belle II precision is reached.

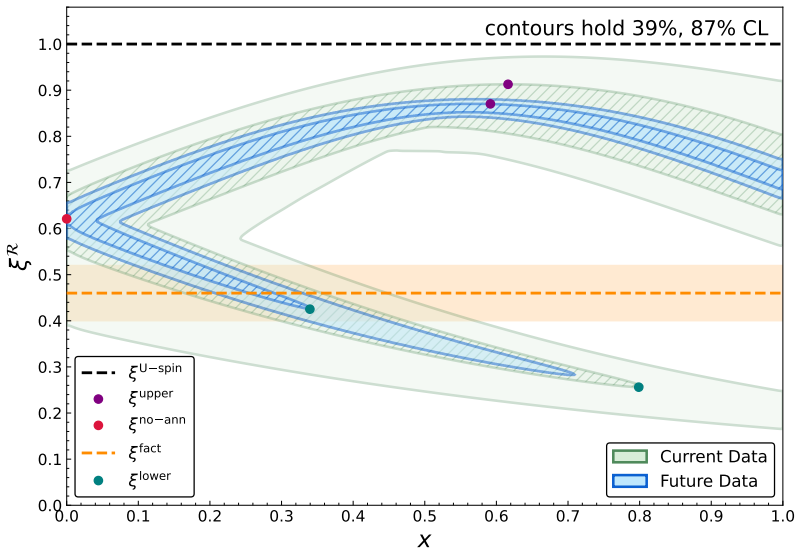

Figure 24: 39% (hatched) and 87% (filled) CL regions obtained with `GammaCombo` *for the E+A+R Fit with $\xi^{\mathcal{R}}$ treated as a free parameter, for the current dataset and the projected future scenario based on the expected end-of-HL-LHC and Belle II precision.*

Figure 24 shows that the allowed confidence-level regions are significantly reduced with respect to the current-data case. From the 39% CL contour, we obtain the extremal points

$$(x, \xi^{\text{upper}}) = (0.59,\, 0.87), \tag{123}$$

$$(x, \xi^{\text{lower}}) = (0.34,\, 0.43). \tag{124}$$

This shows that the projected experimental precision substantially tightens the constraints on $\xi^{\mathcal{R}}$, with ξ^{lower} now overlapping with ξ^{fact}. Nevertheless, the allowed interval remains relatively broad and still no unique determination of $\xi^{\mathcal{R}}$ is possible.

For κ, once the experimental uncertainties are reduced to the projected end-of-HL-LHC and Belle II level, its precision becomes increasingly limited by the form-factor uncertainties entering ξ^{fact}. Since it is difficult to predict how much these uncertainties will improve in the future, we consider a simple benchmark scenario in which the uncertainties of the form factors in Eqs. (87) and (86) are both reduced by a factor of 2, while their central values are kept fixed. This gives

$$\xi^{\text{fact}} = 0.47 \pm 0.03. \tag{125}$$

The resulting contour in the (x, κ) plane is shown in Fig. 25.

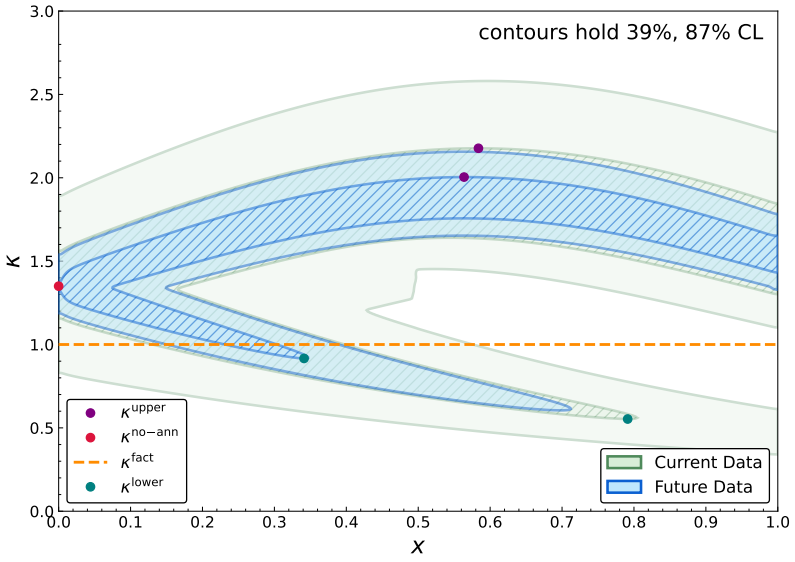

Figure 25: 39% (hatched) and 87% (filled) CL regions obtained with `GammaCombo` *for the E+A+R Fit, comparing the current dataset with the projected future scenario based on the expected end-of-HL-LHC and Belle II precision. For the projected future scenario, a benchmark reduction of the form-factor uncertainties by a factor of 2 is assumed.*

From the 39% CL contour we then find

$$(x, \kappa^{\text{upper}}) = (0.56,\, 2.00), \tag{126}$$

$$(x, \kappa^{\text{lower}}) = (0.34,\, 0.92). \tag{127}$$

Compared with the current situation, the allowed region is again significantly reduced, although it still spans a sizable range in κ.

The values of $\xi^{\mathcal{R}}$ and κ for the current and future datasets are summarized in Table 8 below.

Quantity	Current dataset	Future dataset
ξ^{upper}	0.91	0.87
ξ^{lower}	0.26	0.43
κ^{upper}	2.18	2.00
κ^{lower}	0.56	0.92

Table 8: Summary of the upper and lower values extracted from the 39% CL contours for the current dataset and the projected future scenario based on the expected end-of-HL-LHC and Belle II precision.

Constraint on (x, σ) We now turn to the future E+A+R Fit with Gaussian constraints imposed on $\xi^{\mathcal{R}}$, in order to assess to what extent the annihilation parameters x and σ can be constrained further once the projected experimental precision is reached.

Table 8 shows that the allowed range of $\xi^{\mathcal{R}}$ becomes substantially narrower in the future scenario. However, its lower part still overlaps with the 68% CL interval of the lowest Gaussian constraint considered before, $\xi^{\mathcal{R}} = 0.50 \pm 0.05$.

Similarly, the upper value, $\xi^{\text{upper}} = 0.87$, lies within the 95% CL interval of the highest Gaussian constraint considered before, $\xi^{\mathcal{R}} = 0.80 \pm 0.05$. For this reason, and to maintain a direct comparison with the current-data analysis, we continue to use the same Gaussian constraints as before.

For this future E+A+R Fit, we use the same values for the fit parameters as for the future E+A Fit, taken from Table 2, except for x and σ, which are taken from Table 4. Consequently, only $\overline{\mathcal{R}}$ and the direct CP asymmetries of $B^+ \to J/\psi\pi^+$ and $B^+ \to J/\psi K^+$ have to be recalculated. The resulting best-fit values and projected uncertainties are summarized in Table 9, while the corresponding projected observables are collected in Table E.2 in the Appendix.

$\xi^{\mathcal{R}}$	x	$\sigma\,[^\circ]$	a_{sca}	$\theta_{\text{sca}}\,[^\circ]$	$\phi_d\,[^\circ]$
0.50 ± 0.05	$0.21^{+0.10}_{-0.09}$	$-175.1^{+8.3}_{-4.9}$	$0.135^{+0.034}_{-0.030}$	$166.9^{+7.4}_{-8.1}$	$45.67^{+0.29}_{-0.27}$
0.60 ± 0.05	$0.048^{+0.084}_{-0.046}$	-157^{+139}_{-23}	$0.135^{+0.034}_{-0.030}$	$166.9^{+7.7}_{-8.1}$	$45.67^{+0.29}_{-0.27}$
0.70 ± 0.05	$0.12^{+0.09}_{-0.08}$	$-10.9^{+9.7}_{-27.5}$	$0.135^{+0.034}_{-0.030}$	$167.0^{+7.6}_{-8.2}$	$45.67^{+0.29}_{-0.27}$
0.80 ± 0.05	$0.29^{+0.13}_{-0.10}$	$-4.5^{+4.0}_{-5.2}$	$0.135^{+0.034}_{-0.030}$	$166.9^{+7.7}_{-8.1}$	$45.67^{+0.29}_{-0.27}$
	$0.84^{+0.10}_{-0.13}$	$-1.6^{+1.6}_{-8.2}$	$0.135^{+0.034}_{-0.030}$	$166.9^{+7.7}_{-8.1}$	$45.67^{+0.29}_{-0.27}$

Table 9: Central values and asymmetric uncertainties obtained for different Gaussian inputs of $\xi^{\mathcal{R}}$ in the projected future scenario based on the expected end-of-HL-LHC and Belle II precision.

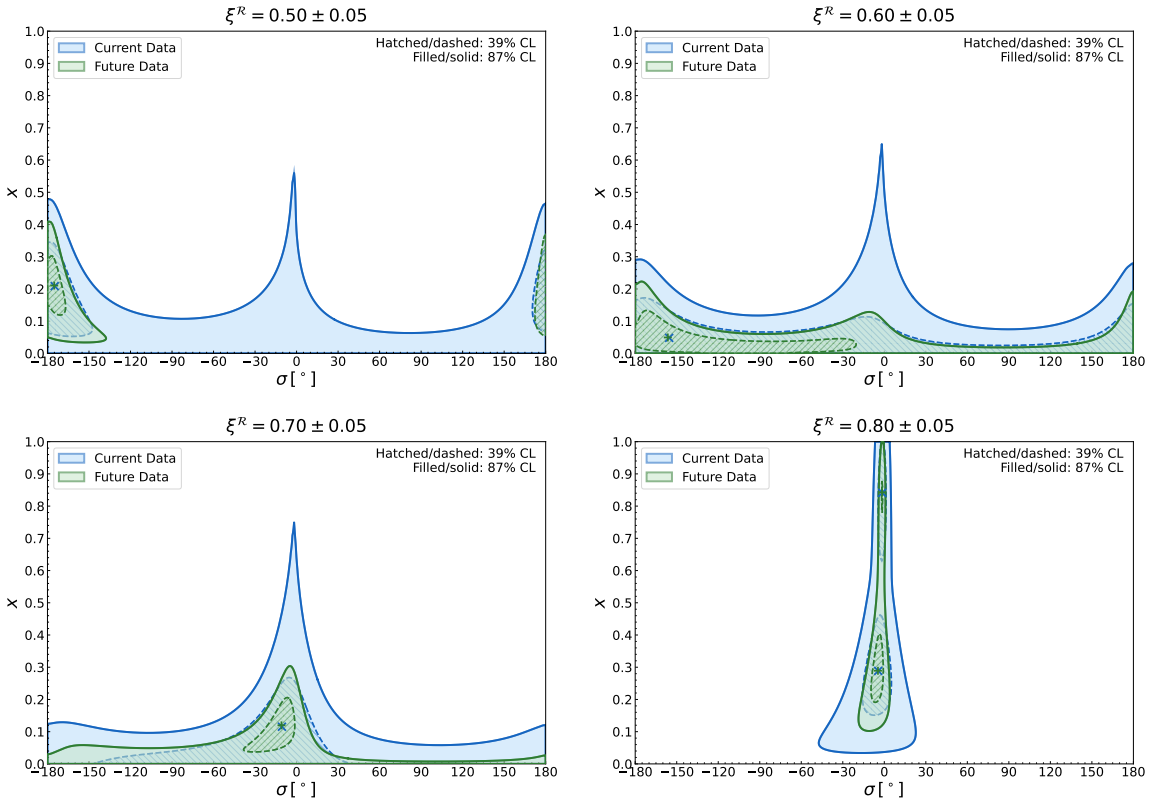

Figure 26: 39% (hatched) and 87% (filled) CL regions for the annihilation parameters, obtained with `GammaCombo` *for the four Gaussian constraints on $\xi^{\mathcal{R}}$. The current dataset is compared with the projected future scenario based on the expected end-of-HL-LHC and Belle II precision.*

A direct comparison with the current-data case is shown in Fig. 26. For all values of $\xi^{\mathcal{R}}$, the projected contour regions are significantly smaller than the corresponding current-data contours, showing a clear reduction of the allowed (x, σ) parameter space.

The improvement can be quantified using the 68% interval-width definition of Eq. (101). Table 10 summarizes the ratios of the future and current-data interval widths for x and σ.

$\xi^{\mathcal{R}}$	$\Delta^{68}_{\rm fut}(x)/\Delta^{68}_{\rm cur}(x)$	$\Delta^{68}_{\rm fut}(\sigma)/\Delta^{68}_{\rm cur}(\sigma)$
0.50 ± 0.05	0.63	0.41
0.60 ± 0.05	0.75	0.45
0.70 ± 0.05	0.63	0.10
0.80 ± 0.05	0.71	0.43
	0.59	0.46
Average	0.66	0.37

Table 10: Comparison of the current-data and projected-future 68% interval widths, denoted by Δ^{68}_{cur} and Δ^{68}_{fut}, respectively, for the annihilation parameters x and σ in the E+A+R Fit. The projected future scenario is based on the expected end-of-HL-LHC and Belle II precision.

Table 10 shows quantitatively that the future projections significantly reduce the allowed 68% interval widths for both x and σ. On average, this corresponds to an improvement by roughly a factor of 1.5 for x and a factor of 2.7 for σ. Overall, the future E+A+R configuration therefore leads to a clear tightening of the constraints on the annihilation parameters. Nevertheless, the constraints in the (x, σ) plane are still not sufficiently strong to definitively establish the naive hierarchy $x \ll a_{\rm sca}$.

8 Conclusion

In this thesis, we investigated what can currently be learned about contributions from annihilation topologies in the charged control modes $B^+ \to J/\psi\pi^+$ and $B^+ \to J/\psi K^+$, and how these contributions affect the determination of the B^0_d–$\bar{B}^0_d$ mixing phase ϕ_d. To this end, we extended the global-fit methodology of Ref. [5] by including contributions from annihilation topologies, encoded by the parameters x and σ.

Using the reparametrized expressions for the CP asymmetries of the B^+ modes in the resulting E+A Fit, we find that the current CP-asymmetry measurements alone do not provide enough complementary information to determine x and σ uniquely. Notably, the case $x = 0$, corresponding to the baseline Extended Fit, remains fully compatible with the current data.

Despite this underconstrained behavior, the impact of annihilation topologies on ϕ_d is found to be limited. In the floating-fit strategy, where x and σ are treated as free fit parameters, the shift in the best-fit central value with respect to the baseline Extended Fit is only $|\delta\phi_d| = 0.03°$, corresponding to about 1% of the experimental 68% interval width. The fixed-point strategy gives a more conservative estimate, with the systematic uncertainty on ϕ_d associated with annihilation topologies amounting to about 10% of the experimental interval width. Therefore, within the current experimental precision, the impact of annihilation topologies on the determination of ϕ_d is negligible.

Including the ratio of CP-averaged branching fractions $\overline{\mathcal{R}}$, corresponding to the E+A+R Fit, significantly improves the constraints on the annihilation parameters and allows unique best-fit values of x and σ to be obtained when the hadronic-amplitude ratio $\xi^{\mathcal{R}}$ is imposed as an external Gaussian constraint. However, these constraints remain limited by the lack of orthogonality between the constraints from the CP asymmetries and $\overline{\mathcal{R}}$. Furthermore, the preferred values of x and σ depend strongly on the assumed value of $\xi^{\mathcal{R}}$. Therefore, a more precise determination of $\xi^{\mathcal{R}}$ is essential if $\overline{\mathcal{R}}$ is to be used as an additional input.

Using future projections based on the expected end-of-HL-LHC and Belle II luminosities, we find that the improved experimental precision significantly tightens the constraints on the fit parameters in both the E+A and E+A+R Fits. Nevertheless, in the E+A Fit, the annihilation parameters remain underconstrained, since the future projections do not change the limited orthogonality of the CP-asymmetry constraints. Similarly, in the E+A+R Fit, the projected confidence-level regions are not yet sufficient to definitively establish the hierarchy $x \ll a_{\text{sca}}$. Applying the fixed-point strategy, we find that the systematic uncertainty on ϕ_d associated with annihilation topologies amounts to 12% of the experimental 68% interval width.

Overall, these findings show that annihilation topologies in the charged control modes can be incorporated consistently in the global-fit framework. Although it remains very challenging to determine the annihilation parameters x and σ precisely, their impact on ϕ_d is negligible compared with the experimental precision, both with current data and with the projected end-of-HL-LHC and Belle II precision. This supports the treatment adopted in Ref. [5], where annihilation topologies in the B^+ modes are neglected in the global-fit strategy.

Acknowledgements

I would first like to thank Kristof de Bruyn, my first supervisor, for introducing me to this fascinating research topic and for his continuous willingness to help throughout the project, which has been an invaluable support. I greatly appreciated the freedom to explore different directions within the research, and I enjoyed discovering the world that lies beyond penguins.

I would also like to thank my second supervisor, Robert Fleischer, and Eleftheria Malami for their time, feedback, and insightful discussions during our meetings. Their input helped me to better understand the broader context of this research and to see how my work fits into the wider picture.

Finally, I would like to thank the LHCb group in Groningen for making the research process so enjoyable. I greatly enjoyed the lunches and coffee breaks together. A special thanks goes to Franca Maat, my officemate, for sharing both the good moments and the difficult times throughout this research.

References

[1] A. Crivellin and B. Mellado, "Anomalies in particle physics and their implications for physics beyond the standard model," *Nature Reviews Physics*, vol. 6, no. 5, pp. 294–309, 2024. DOI: 10.1038/s42254-024-00703-6. arXiv: 2309.03870 [hep-ph].

[2] M. B. Gavela, P. Hernández, J. Orloff, and O. Pène, "Standard model CP-violation and baryon asymmetry," *Modern Physics Letters A*, vol. 9, no. 9, pp. 795–809, 1994. DOI: 10.1142/S0217732394000629. arXiv: hep-ph/9312215 [hep-ph].

[3] C. Linn, "First minimum bias physics results at LHCb," in *Proceedings of the XVI International Symposium on Very High Energy Cosmic Ray Interactions*, Invited talk at ISVHECRI 2010, 2010. arXiv: 1011.2720 [hep-ex].

[4] K. De Bruyn, "Searching for penguin footprints: Towards high precision CP violation measurements in the B meson systems," Ph.D. thesis, Vrije Universiteit Amsterdam, Sep. 2015. [Online]. Available: https://research.vu.nl/en/publications/searching-for-penguin-footprints-towards-high-precision-cp-violat.

[5] K. De Bruyn, R. Fleischer, and E. Malami, "How to tame penguins: Advancing to high-precision measurements of ϕ_d and ϕ_s," *European Physical Journal C*, vol. 86, no. 3, 2026, Art. no. 215. DOI: 10.1140/epjc/s10052-026-15401-z. arXiv: 2505.06102 [hep-ph].

[6] K. De Bruyn, R. Fleischer, E. Malami, and P. van Vliet, "New physics in $B_q^0 - \bar{B}_q^0$ mixing: Present challenges, prospects, and implications for $B_q^0 \to \mu^+\mu^-$," *Journal of Physics G: Nuclear and Particle Physics*, vol. 50, no. 4, 2023, Art. no. 045003. DOI: 10.1088/1361-6471/acab1d. arXiv: 2208.14910 [hep-ph].

[7] S. Sahoo, C. K. Das, and L. Maharana, "The prediction of mass of Z'-boson from $B_q^0 - \bar{B}_q^0$ mixing," *International Journal of Modern Physics A*, vol. 26, no. 20, pp. 3347–3356, 2011. DOI: 10.1142/S0217751X11053936. arXiv: 1112.0460 [hep-ph].

[8] S. Schacht, "Charm CP violation and searches," in *Proceedings of the 58th Rencontres de Moriond on Electroweak Interactions and Unified Theories*, 2024. arXiv: 2405.09299 [hep-ph].

[9] M. Gronau, D. London, and J. L. Rosner, "Rescattering contributions to rare B-meson decays," *Physical Review D*, vol. 87, no. 3, 2013, Art. no. 036008. DOI: 10.1103/PhysRevD.87.036008. arXiv: 1211.5785 [hep-ph].

[10] S. Stone, *B phenomenology*, Lectures presented at the 55th Scottish Universities Summer School in Physics on Heavy Flavour Physics, 2001. arXiv: hep-ph/0112008 [hep-ph].

[11] GammaCombo, *GammaCombo documentation*, 2016. Accessed: Jun. 9, 2026. [Online]. Available: https://gammacombo.github.io/documentation.html.

[12] A. Pich, "Flavour physics and CP violation," in *Proceedings of the 2011 CERN–Latin-American School of High-Energy Physics*, C. Grojean, M. Mulders, and M. Spiropulu, Eds., Geneva: CERN, 2013, pp. 119–144. DOI: 10.5170/CERN-2013-003.119. arXiv: 1112.4094 [hep-ph].

[13] Particle Data Group, S. Navas, et al., "Review of particle physics," *Physical Review D*, vol. 110, no. 3, 2024, Art. no. 030001, ISSN: 2470-0010. DOI: 10.1103/PhysRevD.110.030001.

[14] G. Buchalla, A. J. Buras, and M. E. Lautenbacher, "Weak decays beyond leading logarithms," *Reviews of Modern Physics*, vol. 68, no. 4, pp. 1125–1144, 1996. DOI: 10.1103/RevModPhys.68.1125. arXiv: hep-ph/9512380 [hep-ph].

[15] E. Witten, "Short distance analysis of weak interactions," *Nuclear Physics B*, vol. 122, no. 1, pp. 109–143, 1977, ISSN: 0550-3213. DOI: 10.1016/0550-3213(77)90428-X.

[16] H.-Y. Cheng, "The $\Delta I = 1/2$ rule in kaon decays: A new look," *Chinese Journal of Physics*, vol. 38, p. 783, 2000. arXiv: hep-ph/9906403 [hep-ph].

[17] T. Feldmann, "Non-leptonic heavy meson decays: Theory status," in *Proceedings of the 12th Conference on Flavor Physics and CP Violation*, 2014. arXiv: 1408.0300 [hep-ph].

[18] M. Neubert and B. Stech, "Non-leptonic weak decays of B mesons," in *Heavy Flavours II*, ser. Advanced Series on Directions in High Energy Physics, A. J. Buras and M. Lindner, Eds., vol. 15, World Scientific, 1998, pp. 294–344. DOI: 10.1142/9789812812667_0004. arXiv: hep-ph/9705292 [hep-ph].

[19] S. Mantry, D. Pirjol, and I. W. Stewart, "Strong phases and factorization for color-suppressed decays," *Physical Review D*, vol. 68, no. 11, 2003, Art. no. 114009. DOI: 10.1103/PhysRevD.68.114009. arXiv: hep-ph/0306254 [hep-ph].

[20] A. Ali and V. M. Braun, "Estimates of the weak annihilation contributions to the decays $B \to \rho^+\gamma$ and $B \to \omega\gamma$," *Physics Letters B*, vol. 359, no. 1–2, pp. 223–235, 1995. DOI: 10.1016/0370-2693(95)01087-7. arXiv: hep-ph/9506248 [hep-ph].

[21] A. J. Buras, J.-M. Gérard, and R. Rückl, "1/N expansion for exclusive and inclusive charm decays," *Nuclear Physics B*, vol. 268, no. 1, pp. 16–48, 1986, ISSN: 0550-3213. DOI: 10.1016/0550-3213(86)90200-2.

[22] M. Beneke and M. Neubert, "QCD factorization for $B \to PP$ and $B \to PV$ decays," *Nuclear Physics B*, vol. 675, no. 1–2, pp. 333–415, 2003. DOI: 10.1016/j.nuclphysb.2003.09.026. arXiv: hep-ph/0308039 [hep-ph].

[23] H.-Y. Cheng, C.-K. Chua, and A. Soni, "Final state interactions in hadronic B decays," *Physical Review D*, vol. 71, no. 1, 2005, Art. no. 014030. DOI: 10.1103/PhysRevD.71.014030. arXiv: hep-ph/0409317 [hep-ph].

[24] H.-Y. Cheng and K.-C. Yang, "Updated analysis of a_1 and a_2 in hadronic two-body decays of B mesons," *Physical Review D*, vol. 59, no. 9, 1999, Art. no. 092004. DOI: 10.1103/PhysRevD.59.092004. arXiv: hep-ph/9811249 [hep-ph].

[25] H.-Y. Cheng and K.-C. Yang, "Analysis of $B \to \phi K$ decays in QCD factorization," *Physical Review D*, vol. 64, no. 7, 2001, Art. no. 074004. DOI: 10.1103/PhysRevD.64.074004. arXiv: hep-ph/0012152 [hep-ph].

[26] A. Ali, *Towards a theory of charmless non-leptonic two-body B decays*, 1998. arXiv: hep-ph/9812434 [hep-ph].

[27] W. G. Parrott, C. Bouchard, and C. T. H. Davies, "$B \to K$ and $D \to K$ form factors from fully relativistic lattice QCD," *Physical Review D*, vol. 107, no. 1, 2023, Art. no. 014510, ISSN: 2470-0010. DOI: 10.1103/PhysRevD.107.014510. arXiv: 2207.12468 [hep-lat].

[28] B.-Y. Cui, Y.-K. Huang, Y.-L. Shen, C. Wang, and Y.-M. Wang, "Precision calculations of $B_{d,s} \to \pi, K$ decay form factors in soft-collinear effective theory," *Journal of High Energy Physics*, vol. 2023, no. 3, 2023, Art. no. 140, ISSN: 1029-8479. DOI: 10.1007/JHEP03(2023)140. arXiv: 2212.11624 [hep-ph].

[29] B. Colquhoun, S. Hashimoto, T. Kaneko, and J. Koponen, "Form factors of $B \to \pi\ell\nu$ and a determination of $|V_{ub}|$ with Möbius domain-wall fermions," *Physical Review D*, vol. 106, no. 5, 2022, Art. no. 054502. DOI: 10.1103/PhysRevD.106.054502. arXiv: 2203.04938 [hep-lat].

[30] LHCb Collaboration, I. Bediaga, et al., "Physics case for an LHCb upgrade II: Opportunities in flavour physics, and beyond, in the HL-LHC era," CERN, Tech. Rep. CERN-LHCC-2018-027; LHCb-PUB-2018-009, 2018. arXiv: 1808.08865 [hep-ex].

[31] Belle II Collaboration, E. Kou, et al., "The Belle II physics book," *Progress of Theoretical and Experimental Physics*, vol. 2019, no. 12, 2019, Art. no. 123C01. DOI: 10.1093/ptep/ptz106. arXiv: 1808.10567 [hep-ex].

[32] LHCb Collaboration, R. Aaij, et al., "First evidence for direct CP violation in beauty to charmonium decays," *Physical Review Letters*, vol. 134, no. 10, 2025, Art. no. 101801. DOI: 10.1103/PhysRevLett.134.101801. arXiv: 2411.12178 [hep-ex].

[33] LHCb Collaboration, R. Aaij, et al., "Measurement of the $B^{\pm}$ production asymmetry and the CP asymmetry in $B^{\pm} \to J/\psi K^{\pm}$ decays," *Physical Review D*, vol. 95, no. 5, 2017, Art. no. 052005, ISSN: 2470-0010. DOI: 10.1103/PhysRevD.95.052005. arXiv: 1701.05501 [hep-ex].

[34] M. E. Peskin and D. V. Schroeder, *An Introduction to Quantum Field Theory*. CRC Press, 2019, 842 pp., ISBN: 9780367320560.

[35] I. M. Gel'fand and N. Y. Vilenkin, *Generalized Functions. Volume 4: Applications of Harmonic Analysis*. Academic Press, 1964, 384 pp., Translated by Amiel Feinstein, ISBN: 9781483262246.

[36] Belle II Collaboration, I. Adachi, et al., "New graph-neural-network flavor tagger for Belle II and measurement of $\sin 2\phi_1$ in $B^0 \to J/\psi K^0_S$ decays," *Physical Review D*, vol. 110, no. 1, 2024, Art. no. 012001. DOI: 10.1103/PhysRevD.110.012001. arXiv: 2402.17260 [hep-ex].

[37] LHCb Collaboration, R. Aaij, et al., "Measurement of CP violation in $B^0 \to \psi(\to \ell^+\ell^-)K^0_S(\to \pi^+\pi^-)$ decays," *Physical Review Letters*, vol. 132, no. 2, 2024, Art. no. 021801. DOI: 10.1103/PhysRevLett.132.021801. arXiv: 2309.09728 [hep-ex].

[38] LHCb Collaboration, R. Aaij, et al., "Measurement of the time-dependent CP asymmetries in $B^0_s \to J/\psi K^0_S$," *Journal of High Energy Physics*, vol. 2015, no. 6, 2015, Art. no. 131. DOI: 10.1007/JHEP06(2015)131. arXiv: 1503.07055 [hep-ex].

[39] Belle II Collaboration, I. Adachi, et al., "Observation of time-dependent CP violation and measurement of the branching fraction of $B^0 \to J/\psi\pi^0$ decays," *Physical Review D*, vol. 111, no. 1, 2025, Art. no. 012011. DOI: 10.1103/PhysRevD.111.012011. arXiv: 2410.08622 [hep-ex].

[40] LHCb Collaboration, R. Aaij, et al., "Measurement of the CP-violating phase β in $B^0 \to J/\psi\pi^+\pi^-$ decays and limits on penguin effects," *Physics Letters B*, vol. 742, pp. 38–49, 2015. DOI: 10.1016/j.physletb.2015.01.008. arXiv: 1411.1634 [hep-ex].

Appendix

A Decay Rate Derivation

Here, we derive the expression for the decay rate. The partial decay rate of a particle with mass M into n particles in its rest frame is given by [13]

$$d\Gamma = \frac{(2\pi)^4}{2M} |A|^2 \, d\Phi_n(P; p_1, \ldots, p_n), \tag{A.1}$$

where $A = \langle f|\mathcal{H}|i\rangle$ denotes the invariant decay amplitude, P is the four-momentum of the decaying particle, p_i are the four-momenta of the final-state particles, and $d\Phi_n$ is the n-body phase-space element, given by

$$d\Phi_n(P; p_1, \ldots, p_n) = \delta^4 \left(P - \sum_{i=1}^{n} p_i \right) \prod_{i=1}^{n} \frac{d^3 p_i}{(2\pi)^3 2E_i}. \tag{A.2}$$

Here, E_i is the energy of the ith final-state particle. The delta function ensures conservation of energy and momentum.

It is worth noting that, although this expression is evaluated in the rest frame of the decaying particle, Γ is Lorentz invariant. This follows from the Lorentz invariance of $|A|^2$, the mass M, and the phase-space measure $d^3p_i/[(2\pi)^3 2E_i]$ [34]. Hence, the result obtained in the rest frame gives the general expression for the decay width.

For a two-body decay, it follows that the decay rate is given by

$$\begin{aligned} \Gamma &= \frac{(2\pi)^4}{2M} |A|^2 \iint \delta(M - E_1 - E_2) \delta^3(\vec{p_1} + \vec{p_2}) \frac{d^3\vec{p_1}}{(2\pi)^3 2E_1} \frac{d^3\vec{p_2}}{(2\pi)^3 2E_2} \\ &= \frac{(2\pi)^4}{2M} |A|^2 \int \delta(M - E_1 - E_2) \frac{|\vec{p_1}|^2 d|\vec{p_1}| d\Omega}{(2\pi)^3 2E_1} \frac{1}{(2\pi)^3 2E_2} \Big|_{\vec{p_2} = -\vec{p_1}}, \end{aligned} \tag{A.3}$$

where Ω is the solid angle of particle 1.

We can now employ the following identity for the delta function [35]:

$$\delta(f(x)) = \sum_i \frac{\delta(x - x_i)}{|f'(x_i)|}, \tag{A.4}$$

where $f(x_i) = 0$.

Define $|\vec{p}_*|$ such that $f(|\vec{p}_*|) = M - E_1(|\vec{p}_*|) - E_2(|\vec{p}_*|) = 0$. It follows from Eq. (A.4) that the delta function can be rewritten as

$$\delta(M - E_1 - E_2)\Big|_{\vec{p_2} = -\vec{p_1}} = \frac{\delta(|\vec{p_1}| - |\vec{p}_*|)}{|\vec{p_1}|(E_1 + E_2)} E_1 E_2. \tag{A.5}$$

Hence, to obey four-momentum conservation, we have $|\vec{p_1}| = |\vec{p}_*| = |\vec{p_2}|$, given by

$$|\vec{p_1}| = |\vec{p_2}| = \frac{1}{2M} \sqrt{\lambda(M^2, m_1^2, m_2^2)}, \tag{A.6}$$

where $\lambda(a, b, c) \equiv a^2 + b^2 + c^2 - 2ab - 2ac - 2bc$ is the Källén function [13] and $M = E_1 + E_2$.

The decay rate is then finally given by [13]

$$\Gamma = \frac{1}{32\pi^2} \frac{|\vec{p}_1|}{M^2} \int d\Omega \, |A|^2. \tag{A.7}$$

In general, the squared matrix element $|A|^2$ may depend on the solid angle Ω. For an isotropic decay, however, $|A|^2$ is independent of Ω, such that the angular integration gives $\int d\Omega = 4\pi$. The decay rate then reduces to

$$\Gamma = \frac{1}{8\pi} |A|^2 \frac{|\vec{p}_1|}{M^2}. \tag{A.8}$$

B Derivation Kinematic Factor

Since the contraction $\epsilon_\mu^*(p_B + p_P)^\mu$ is Lorentz invariant, the decay can be analyzed in the rest frame of the B meson. In general, the three-momenta of the final-state particles $\vec{p}_V$ and $\vec{p}_P$ can point in any direction, as long as they are antiparallel, which follows from momentum conservation. Hence, we can parametrize the momenta as

$$p_B^\mu = R^\mu{}_\nu p_{B,z}^\nu, \quad p_V^\mu = R^\mu{}_\nu p_{V,z}^\nu, \quad p_P^\mu = R^\mu{}_\nu p_{P,z}^\nu, \tag{B.1}$$

where

$$p_{B,z}^\mu = (m_B, \vec{0}), \quad p_{V,z}^\mu = (E_V, 0, 0, |\vec{p}_P|), \quad p_{P,z}^\mu = (E_P, 0, 0, -|\vec{p}_P|), \tag{B.2}$$

are the four-momenta in the configuration where $\vec{p}_V$ points in the $+z$-direction, and $R^\mu{}_\nu$ is a general rotation. The rotation does not affect p_B^μ since the B meson is at rest.

From Eq. (69), it follows that

$$|\vec{p}_P| = \frac{1}{2m_B}\sqrt{\lambda\left(m_B^2, m_V^2, m_P^2\right)} = |\vec{p}_V|, \tag{B.3}$$

$$E_V(|\vec{p}_P|) = \sqrt{|\vec{p}_P|^2 + m_V^2}, \quad E_P(|\vec{p}_P|) = \sqrt{|\vec{p}_P|^2 + m_P^2}. \tag{B.4}$$

The polarization vector of the vector meson in the helicity basis, assuming motion in the $+z$-direction, is given by

$$(\epsilon_z)_\mu(\vec{p}_V; \pm) = \frac{1}{\sqrt{2}}(0, 1, \pm i, 0), \quad (\epsilon_z)_\mu(\vec{p}_V; 0) = \frac{1}{m_V}\left(-|\vec{p}_P|, 0, 0, E_V\right), \tag{B.5}$$

where $\lambda = \pm 1$ corresponds to transverse polarizations and $\lambda = 0$ to longitudinal polarization. In particular, the polarization vectors $(\epsilon_z)_\mu$ are eigenstates of the rotation matrix $R_z(\theta)$ around the z-axis:

$$(R_z)_\mu{}^\nu(\theta)(\epsilon_z)_\nu(\vec{p}_V, \lambda) = e^{i\lambda\theta}(\epsilon_z)_\mu(\vec{p}_V, \lambda), \tag{B.6}$$

where

$$(R_z)_\mu{}^\nu(\theta) = \begin{pmatrix} 1 & 0 & 0 & 0 \\ 0 & \cos\theta & \sin\theta & 0 \\ 0 & -\sin\theta & \cos\theta & 0 \\ 0 & 0 & 0 & 1 \end{pmatrix}. \tag{B.7}$$

Since $\vec{p}_V$ points in the $R\hat{z}$-direction, we must also apply this rotation to the polarization vector:

$$\epsilon_\mu(\vec{p}_V, \lambda) = R_\mu{}^\nu(\epsilon_z)_\nu(p_{V,z}, \lambda). \tag{B.8}$$

This gives

$$\epsilon^*_\mu(\vec{p}_V, \lambda)(p_B + p_P)^\mu = R_\mu{}^\nu(\epsilon_z)^*_\nu R^\mu{}_\rho(p_{B,z} + p_{P,z})^\rho = (\epsilon_z)^*_\nu(p_{B,z} + p_{P,z})^\nu, \tag{B.9}$$

where we used

$$R_\mu{}^\nu R^\mu{}_\rho = \delta^\nu{}_\rho. \tag{B.10}$$

Equation (B.9) then yields

$$\epsilon^*_\mu(\vec{p}_V, \pm)(p_B + p_P)^\mu = 0, \tag{B.11}$$

$$\epsilon^*_\mu(\vec{p}_V, 0)(p_B + p_P)^\mu = -\frac{|\vec{p}_P|}{m_V}\left(m_B + E_P + E_V\right). \tag{B.12}$$

Using the conservation of energy, this becomes

$$\epsilon^*_\mu(\vec{p}_V, 0)(p_B + p_P)^\mu = -\frac{2m_B|\vec{p}_P|}{m_V}. \tag{B.13}$$

Hence, we get

$$\left|\frac{\epsilon^*_\mu(p_B + p_P)^\mu}{\epsilon'^*_\mu(p_B + p_{P'})^\mu}\right| = \frac{|\vec{p}_P|}{|\vec{p}_{P'}|}. \tag{B.14}$$

C Determination $f_{B\to\pi}^{+}(m_{J/\psi}^2)$

For the evaluation of the $B \to \pi$ form factor, we use the BCL coefficients and their correlation matrix from Ref. [28].

```python
import numpy as np

# Neglect the uncertainties in the masses

# Masses (GeV)
m_B = 5.27941 # GeV - mass of B+
m_Bstar = 5.32475 # GeV
m_pi = 0.13957039 # GeV
m_Jpsi = 3.096900 # GeV

# z-mapping parameters
tplus = (m_B + m_pi)**2
tminus = (m_B - m_pi)**2
t0 = tplus - np.sqrt(tplus*(tplus-tminus))
Nz = 3

# BCL coefficients
b = np.array([0.404, -0.618, -0.473])
sig = np.array([0.013, 0.063, 0.215])

# Correlation matrix  (Table VIII)
rho = np.array([
    [ 1.000, 0.276, -0.446],
    [0.276,  1.000,  -0.374],
    [-0.446,  -0.374,  1.000]
])

# Covariance C_ij = rho_ij sigma_i sigma_j
C = rho * np.outer(sig, sig)

# f+(q^2) and its uncertainty at q^2 = m_J/psi^2
q2 = m_Jpsi**2
pref = 1.0 / (1.0 - q2 / m_Bstar**2)
z = (np.sqrt(tplus - q2) - np.sqrt(tplus - t0)) / (np.sqrt(tplus - q2) +
    np.sqrt(tplus - t0))

A = np.zeros(Nz)
for k in range(Nz):
    A[k] = z**k - ((-1)**(k - Nz)) * (k / Nz) * (z**Nz)

f = pref * np.dot(b, A)
var = (pref**2) * (A @ C @ A)
err = np.sqrt(var)

print(f"f+(m_J/psi^2) = {f:.4f} ± {err:.4f}")
```

D GammaCombo Combiner Module

The combiner module used to perform the fit strategies depicted in Fig. 9 in the `GammaCombo` framework is available in the `Huy26` branch of the following GitLab repository:

https://gitlab.cern.ch/gammacombo/penguinfit/

The directory should be placed inside the main `gammacombo` directory.

To ensure compatibility and reproduce the calculations using the same version of ROOT, the following command can be run in the CERN `lxplus` environment to initialize ROOT 6.32.10:

```
source /cvmfs/sft.cern.ch/lcg/app/releases/ROOT/6.32.10/
x86_64-almalinux9.5-gcc115-opt/bin/thisroot.sh
```

E Future Projections

E.1 Extended and E+A Fit

	Extended Fit	E+A Fit
$\mathcal{A}_{\rm CP}^{\rm dir}(B^+ \to J/\psi\pi^+)$ [32]	$0.0147 \pm 0.0008 \pm 0.0008$	$0.0180 \pm 0.0008 \pm 0.0008$
$\mathcal{A}_{\rm CP}^{\rm dir}(B^+ \to J/\psi K^+)$ [33]	$-0.0009 \pm 0.0003 \pm 0.0007$	$-0.0008 \pm 0.0003 \pm 0.0007$
$\mathcal{A}_{\rm CP}^{\rm dir}(B_d^0 \to J/\psi K^0)$ [36]	$-0.0009 \pm 0.0025 \pm 0.0290$	$-0.0029 \pm 0.0025 \pm 0.0290$
$\eta_{\rm CP}\mathcal{A}_{\rm CP}^{\rm mix}(B_d^0 \to J/\psi K^0)$ [36]	$0.7071 \pm 0.0035 \pm 0.0083$	$0.7065 \pm 0.0035 \pm 0.0083$
ρ [36]	$+0.09$	$+0.09$
$\mathcal{A}_{\rm CP}^{\rm dir}(B_d^0 \to J/\psi K^0)$ [37]	$-0.0009 \pm 0.0020 \pm 0.0030$	$-0.0029 \pm 0.0020 \pm 0.0030$
$\eta_{\rm CP}\mathcal{A}_{\rm CP}^{\rm mix}(B_d^0 \to J/\psi K^0)$ [37]	0.7071 ± 0.0030	0.7065 ± 0.0030
ρ [37]	$+0.437$	$+0.437$
$\mathcal{A}_{\rm CP}^{\rm dir}(B_s^0 \to J/\psi K_S^0)$ [38]	$0.01 \pm 0.03 \pm 0.08$	$0.05 \pm 0.03 \pm 0.08$
$\eta_{\rm CP}\mathcal{A}_{\rm CP}^{\rm mix}(B_s^0 \to J/\psi K_S^0)$ [38]	$0.16 \pm 0.03 \pm 0.08$	$0.16 \pm 0.03 \pm 0.08$
ρ [38]	$+0.06$	$+0.06$
$\mathcal{A}_{\rm CP}^{\rm dir}(B_d^0 \to J/\psi\pi^0)$ [39]	$0.015 \pm 0.010 \pm 0.034$	$0.049 \pm 0.010 \pm 0.034$
$\eta_{\rm CP}\mathcal{A}_{\rm CP}^{\rm mix}(B_d^0 \to J/\psi\pi^0)$ [39]	$0.853 \pm 0.015 \pm 0.032$	$0.854 \pm 0.015 \pm 0.032$
ρ [39]	$+0.08$	$+0.08$
$\mathcal{A}_{\rm CP}^{\rm dir}(B_d^0 \to J/\psi\rho^0)$ [40]	$-0.036 \pm 0.004 \pm 0.019$	$-0.036 \pm 0.004 \pm 0.019$
$\eta_{\rm CP}\mathcal{A}_{\rm CP}^{\rm mix}(B_d^0 \to J/\psi\rho^0)$ [40]	$0.663 \pm 0.009 \pm 0.090$	$0.662 \pm 0.009 \pm 0.090$
ρ [40]	$+0.01$	$+0.01$
$\mathcal{A}_{\rm CP}^{\rm dir}(B_s^0 \to J/\psi\phi)$ [5]	0.0018 ± 0.0016	0.0018 ± 0.0016
$\eta_{\rm CP}\mathcal{A}_{\rm CP}^{\rm mix}(B_s^0 \to J/\psi\phi)$ [5]	-0.0612 ± 0.0039	-0.0612 ± 0.0039
$\mathcal{A}_{\rm CP}^{\rm dir}(B_d^0 \to D^+D^-)$ [5]	-0.002 ± 0.021	-0.002 ± 0.021
$\eta_{\rm CP}\mathcal{A}_{\rm CP}^{\rm mix}(B_d^0 \to D^+D^-)$ [5]	0.705 ± 0.043	0.705 ± 0.043
$\mathcal{A}_{\rm CP}^{\rm dir}(B_s^0 \to D_s^+D_s^-)$ [5]	0.0001 ± 0.0260	0.0001 ± 0.0260
$\eta_{\rm CP}\mathcal{A}_{\rm CP}^{\rm mix}(B_s^0 \to D_s^+D_s^-)$ [5]	-0.0642 ± 0.009	-0.0642 ± 0.009
$\mathcal{A}_{\rm CP}^{\rm dir}(B_s^0 \to J/\psi\bar{K}^{*0})$ [5]	-0.036 ± 0.005	-0.036 ± 0.005

Table E.1: Projected future CP-asymmetry inputs for the Extended Fit and the Extended + Annihilation (E+A) Fit, corresponding to the expected end-of-HL-LHC and Belle II precision. The central values are recalculated using the best-fit values in Table 2. For the CP asymmetries other than those of the B^+ modes, the projected statistical uncertainties are taken from Ref. [5].

E.2 E+A+R Fit

$\xi^{\mathcal{R}}$	$\overline{\mathcal{R}}\,(10^{-2})$	$\mathcal{A}_{\rm CP}^{\rm dir}(B^+ \to J/\psi\pi^+)$	$\mathcal{A}_{\rm CP}^{\rm dir}(B^+ \to J/\psi K^+)$
0.50 ± 0.05	$3.815 \pm 0.003 \pm 0.018$	$0.0160 \pm 0.0008 \pm 0.0008$	$-0.0012 \pm 0.0003 \pm 0.0007$
0.60 ± 0.05	$3.819 \pm 0.003 \pm 0.018$	$0.0156 \pm 0.0008 \pm 0.0008$	$-0.0010 \pm 0.0003 \pm 0.0007$
0.70 ± 0.05	$3.812 \pm 0.003 \pm 0.018$	$0.0138 \pm 0.0008 \pm 0.0008$	$-0.0007 \pm 0.0003 \pm 0.0007$
0.80 ± 0.05	$3.823 \pm 0.003 \pm 0.018$	$0.0149 \pm 0.0008 \pm 0.0008$	$-0.0007 \pm 0.0003 \pm 0.0007$

Table E.2: Projected future inputs for the ratio of CP-averaged branching fractions $\overline{\mathcal{R}}$ and the direct CP asymmetries at the expected end-of-HL-LHC precision, shown for different Gaussian constraints on $\xi^{\mathcal{R}}$. The central values are recalculated using the best-fit values in Table 4. For $\xi^{\mathcal{R}} = 0.80 \pm 0.05$, the best-fit solution corresponding to $(x, \sigma) = (0.29, -4.6^\circ)$ is used.